inventions

MDPI

Article

Effect of Support Stiffness Nonlinearity on the Low-Frequency Vibro-Acoustic Characteristics for a Mechanical Equipment—Floating Raft—Underwater Cylindrical Shell Coupled System

Likang Wang [1,2] and Rui Huo [1,2,*]

[1] School of Mechanical Engineering, Shandong University, Jinan 250061, China; 202134363@mail.sdu.edu.cn
[2] Key Laboratory of High Efficiency and Clean Mechanical Manufacture, Shandong University, Ministry of Education, Jinan 250061, China
* Correspondence: huorui@sdu.edu.cn

Abstract: The low-frequency vibro-acoustic characteristics of a mechanical equipment—floating raft—cylindrical shell—underwater acoustic field coupled system with nonlinear supports are studied in this paper. Firstly, the state space equations were established by a modal superposition theory for the coupled system, and a modal parameter identification method was deduced and verified for the cylindrical shell—underwater acoustic field coupled subsystem. On this basis, the formulas were derived for transmitted power flow in the coupled system, and the nonlinear stiffness constitutive relation of the vibration isolation supports was expressed by softening and hardening characteristics. Finally, dynamic simulations were carried out by the Runge—Kutta method to analyze the effect of nonlinear stiffness characteristic parameters on the low-frequency vibration modes and vibro-acoustic transfer characteristics in the coupled system. The research shows that a superharmonic phenomenon is common in the steady vibration mode of the coupled system with a nonlinear softening (or hardening) stiffness characteristic under harmonic excitation. The stronger the softening (or hardening) stiffness characteristic is, the more complex the vibration form is, and the smaller (or larger) the low-frequency vibro-acoustic transfer level in resonance regions is.

Keywords: support stiffness nonlinearity; cylindrical shell; modal parameter identification; low-frequency vibration; transmitted power flow; vibro-acoustic transfer characteristics

Citation: Wang, L.; Huo, R. Effect of Support Stiffness Nonlinearity on the Low-Frequency Vibro-Acoustic Characteristics for a Mechanical Equipment—Floating Raft—Underwater Cylindrical Shell Coupled System. *Inventions* **2023**, *8*, 118. https://doi.org/10.3390/inventions8050118

Academic Editors: Peng Du, Haibao Hu and Xiaopeng Chen

Received: 11 August 2023
Revised: 13 September 2023
Accepted: 18 September 2023
Published: 21 September 2023

1. Introduction

Nonlinear vibration mode is an important factor to be considered in the study of low-frequency vibration isolation for underwater cylindrical shell systems. Due to relatively high vibration energy at low frequencies, the elastic support, which presents linear stiffness in an original micro-amplitude vibration mode, will show nonlinear characteristics. Strictly speaking, stiffness characteristics of various elastic vibration isolation elements are nonlinear. In a micro-amplitude vibration mode, a vibration isolator has a certain linear stiffness working interval. Stiffness characteristics are nonlinear if amplitude is sufficiently large.

In recent years, many scholars have studied the vibration characteristics of nonlinear vibration isolation systems. Smirnov et al. [1] studied and compared the efficiency of linear and nonlinear vibration isolation systems. Santhosh [2] studied the dynamic performance of an asymmetric nonlinear vibration isolation mechanism under harmonic excitation. Dutta et al. [3] analyzed a nonlinear vibration isolator with magnetorheological fluid dampers and cubic nonlinear springs to determine the effectiveness of isolation during force or displacement excitation. Suman et al. [4] proposed a nonlinear vibration control device based on a negative stiffness mechanism, which can improve the isolation ability of the vibration suspension system in the low-frequency range. Araki et al. [5] proposed a vertical

quasi-zero stiffness (QZS) vibration isolator with adjustable restoring force. Zhao et al. [6,7] successively designed QZS vibration isolators with two and three pairs of inclined springs. Ye et al. [8] proposed a QZS system based on a cam—roller mechanism. Chang et al. [9] proposed a QZS dynamic shock absorber. Bouna et al. [10] studied the vibration control of multi-span girder bridges under the excitation of pier foundation vibration by using nonlinear QZS isolators. Drezet et al. [11] proposed a nonlinear vibration energy harvester based on the concept of high static and low dynamic stiffness (HSLDS). Lu et al. [12–14] studied an orthogonal six-degree-of-freedom vibration isolation system with HSLDS and an electromagnetic Stewart platform to suppress the low-frequency vibration of high-precision instruments, provided modal coefficients by improved Fourier series and the Rayleigh—Ritz method, and studied the nonlinear energy transfer of flexible plates with arbitrary boundaries coupled to HSLDS isolators. Sun et al. [15] proposed a method for designing HSLDS mounts based on target force curves, which are obtained by placing negative stiffness structures in parallel with positive stiffness linear springs. Yao et al. [16] proposed an HSLDS isolator with a cam—roller—spring mechanism, in which the cam profile can be specially designed to suit different operating requirements. Chong et al. [17] designed a nonlinear X-combined structure with HSLDS in a large displacement range, which avoided negative stiffness and instability factors and improved its vibration isolation characteristics.

Chaos is a unique dynamical behavior of nonlinear systems. Leutcho et al. [18] systematically studied a new type of chaotic system with single parametric nonlinearity. Yan et al. [19] proposed a novel bi-state nonlinear vibration isolator, whose motion can be either periodic or chaotic. Rahman et al. [20] proposed a new fractional-order chaotic system containing multiple nonlinear terms, which can excite hidden chaotic attractors or self-excited chaotic attractors depending on the chosen system parameters or the value of its fractional-order derivative. Li et al. [21] proposed an SRN feature extraction method combining maximum relevance minimum redundancy, which can effectively classify different chaotic signals. Karimov et al. [22] proposed a novel implementation of the chaotic Duffing oscillator as a simple mechanical system with a translational movement. Dreau et al. [23] introduced a stochastic modeling method for nonlinear systems with response surface discontinuity, which improved the efficiency of multi-variate polynomial chaos expansion.

The power flow characteristic is an important index to study nonlinear vibration isolation. Cassidy et al. [24] proposed a general nonlinear control synthesis method for power flow constrained energy harvesters, which is analytically guaranteed to be superior to the optimal static admittance in the steady state random response. Silva et al. [25] proposed a technique for evaluating and optimizing vibrational power flow involving beam-and-plate coupling. Varghese et al. [26] applied the combined transient power flow balancing and acceleration matching techniques to detect and quantify the crack damage of beam structures at different positions. Yang et al. [27,28] successively studied the power flow and force transmissibility characteristics of a two-degree-of-freedom nonlinear vibration isolation system and a coupled nonlinear oscillator. Ren et al. [29] compared the power transmission between rigid, single-stage isolation and double-stage isolation gearbox installation configurations with the vibration power flow of the system as the evaluation index. Zhang et al. [30] proposed a power flow analysis method for quantitatively evaluating the dynamic performance of a nonlinear energy sink in the frequency domain. Xu et al. [31] analyzed the bending vibration and power flow of axially loaded beams with arbitrary boundaries and nonuniform elastic foundations via energy principle in conjunction with the Rayleigh—Ritz procedure. Mahapatra et al. [32] studied the influence of general coupling conditions on the vibration and power flow characteristics of a two-plate composite plate structure.

There has been a lot of literature on the dynamics of nonlinear vibration isolation systems at home and abroad and, especially, the application of quasi-zero stiffness or high static and low dynamic stiffness nonlinear vibration isolators for low-frequency vibration control has become a research hotspot in the last decade. However, compared with the wide application of nonlinear vibration isolators, the mechanism of vibro-acoustic transfer

in nonlinear vibration isolation systems, especially the influence of nonlinear factors in low-frequency vibration modes, has not been fully studied. In this paper, the low-frequency vibro-acoustic characteristics of a mechanical equipment—floating raft—underwater cylindrical shell coupled system with nonlinear stiffness supports are studied. It can not only provide theoretical guidance for low-frequency vibration analysis, diagnosis, and design of dynamics of underwater nonlinear coupled systems but also provide reference for the design of nonlinear vibration isolators.

The rest of this paper is organized as follows. In Section 2, based on the parametric modeling of an admittance method of a mechanical equipment—floating raft—cylindrical shell—underwater acoustic field coupled system, the state space equations of the subsystems are established by using modal identification and modal superposition theories; and then the nonlinear stiffness constitutive relation of the vibration isolation supports is expressed by softening and hardening characteristics, and the calculation method of transmitted power flow is derived. In Section 3, the influence of nonlinear stiffness characteristic parameters on the vibro-acoustic characteristics of the coupled system is studied by using MATLAB numerical simulation. Finally, some conclusions are presented in Section 4.

2. Materials and Methods

2.1. Model of a Mechanical Equipment—Floating Raft—Cylindrical Shell—Underwater Acoustic Field Coupled System

Figure 1 describes the model of a mechanical equipment—floating raft—cylindrical shell—underwater acoustic field coupled system.

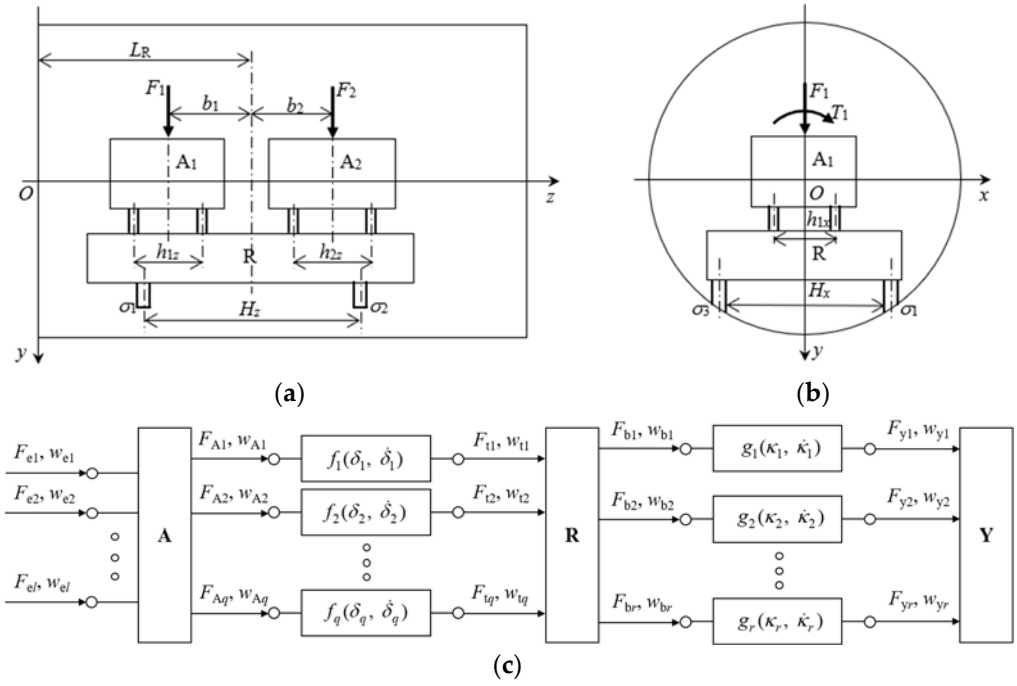

Figure 1. The model of a mechanical equipment—floating raft—cylindrical shell—underwater acoustic field coupled system: (**a**) $-x$ direction; (**b**) z direction; (**c**) complex coupled system with nonlinear connecting elements.

As shown in Figure 1a,b, vibration source mechanical equipment A_1 and A_2 (simulating multiple units) are installed on a floating raft R. Each unit is connected to the raft frame through four elastic supports, and the raft frame is connected to a cylindrical shell through four elastic supports. A rectangular coordinate system *Oxyz* is established, where the *Oz* axis is the center line of the cylinder and *Oy* is the vertical direction. To simplify analysis, only the vertical translational vibration and the rotational vibration around the *Oz* and *Ox* axes of the system are considered. Therefore, vertical excitation forces F_1, F_2

and excitation torques T_1, T_2 around the Oz axis are applied at the center of mass of each unit. The units A_1, A_2 and the floating raft R are all rigid bodies symmetrical about the yOz plane. In Figure 1a,b, b_1, b_2, h_{1z}, h_{2z}, h_{1x}, h_{2x}, H_z, H_x, and L_R are the installation size parameters of the system, and σ_1, σ_2, σ_3, and σ_4 are the connection points of the lower vibration isolation supports with the cylindrical shell.

Figure 1c abstracts the complex coupled system with nonlinear connecting elements. **A** (the vibration source subsystem) is subjected to l excitations F_{en} (n = 1, 2, …, l) and has displacement responses w_{en} at the excitations. **A** is connected to **R** (the raft frame) by q elastic connecting elements. At the connection points of the elastic elements with **A** and **R**, there are excitation forces F_{Ai} and F_{ti} (i = 1, 2, …, q), as well as displacement responses w_{Ai} and w_{ti}. The elastic elements have constitutive relation $f_i(\delta_i, \dot{\delta}_i)$, where $\delta_i = w_{Ai} - w_{ti}$. Similarly, **R** is connected to **Y** (the cylindrical shell–underwater acoustic field coupled subsystem) by r elastic connecting elements. At the connection points of the elastic elements with **R** and **Y**, there are excitation forces F_{bj} and F_{yj} (j = 1, 2, …, r), as well as displacement responses w_{bj} and w_{yj}. The elastic elements have constitutive relation $g_j(\kappa_j, \dot{\kappa}_j)$, where $\kappa_j = w_{bj} - w_{yj}$. For specific practical problems, the number of elastic coupled elements in series in Figure 1c can be increased or decreased according to different modeling needs.

2.2. State Space Model of the Coupled System

For the unit A_1 in Figure 1, its vertical vibration displacement is represented by y_1; its angular displacement around the Ox axis is represented by θ_{1x}; and its angular displacement around the Oy axis is represented by θ_{1y}. Define a state variable $\boldsymbol{u}_{A1} = [u_1, u_2, u_3, u_4, u_5, u_6]^T = [y_1, \theta_{1x}, \theta_{1z}, \dot{y}_1, \dot{\theta}_{1x}, \dot{\theta}_{1z}]^T$, then the state space of the unit A_1 equation is

$$\dot{\boldsymbol{u}}_{A1} = \begin{bmatrix} \dot{u}_1 \\ \dot{u}_2 \\ \dot{u}_3 \\ \dot{u}_4 \\ \dot{u}_5 \\ \dot{u}_6 \end{bmatrix} = \begin{bmatrix} 0 & 0 & 0 & 1 & 0 & 0 \\ 0 & 0 & 0 & 0 & 1 & 0 \\ 0 & 0 & 0 & 0 & 0 & 1 \\ 0 & 0 & 0 & 0 & 0 & 0 \\ 0 & 0 & 0 & 0 & 0 & 0 \\ 0 & 0 & 0 & 0 & 0 & 0 \end{bmatrix} \begin{bmatrix} u_1 \\ u_2 \\ u_3 \\ u_4 \\ u_5 \\ u_6 \end{bmatrix} + \begin{bmatrix} 0 \\ 0 \\ 0 \\ -\boldsymbol{I}_{1\times4}\cdot\boldsymbol{F}_1/m_1 \\ \boldsymbol{Z}_1\cdot\boldsymbol{F}_1/J_{1x} \\ -\boldsymbol{X}_1\cdot\boldsymbol{F}_1/J_{1z} \end{bmatrix} + \begin{bmatrix} 0 \\ 0 \\ 0 \\ F_1/m_1 \\ 0 \\ T_1/J_{1z} \end{bmatrix} = \boldsymbol{\Lambda}_0\cdot\boldsymbol{u}_{A1} + \boldsymbol{f}_{A1}(\boldsymbol{F}_1) + \boldsymbol{f}_{in1}(t) \quad (1)$$

where $\boldsymbol{F}_1 = [F_{A1}, F_{A2}, F_{A3}, F_{A4}]^T$ is an excitation force column vector of the unit A_1 to its four supports; m_1, J_{1x}, and J_{1z} are the mass of the unit A_1 and the moment of inertia that bypasses its centroid and is parallel to the axis of Ox and Oz, respectively; $\boldsymbol{X}_1 = [0.5h_{1x}, 0.5h_{1x}, -0.5h_{1x}, -0.5h_{1x}]$; $\boldsymbol{Z}_1 = [-0.5h_{1z}, 0.5h_{1z}, -0.5h_{1z}, 0.5h_{1z}]$; $\boldsymbol{I}_{1\times4}$ denotes a 4-dimensional row vector with all elements 1; $\boldsymbol{f}_{A1}(\boldsymbol{F}_1)$ denotes a vector function with respect to $\boldsymbol{F}_1$; $\boldsymbol{f}_{in1}$ is a known external input vector function; $\boldsymbol{\Lambda}_0$ is a constant matrix.

Similarly, for the unit A_2, its vertical vibration displacement is represented by y_2; its angular displacement around the Ox axis is represented by θ_{2x}; and its angular displacement around the Oy axis is represented by θ_{2y}. Define a state variable $\boldsymbol{u}_{A2} = [u_7, u_8, u_9, u_{10}, u_{11}, u_{12}]^T = [y_2, \theta_{2x}, \theta_{2z}, \dot{y}_2, \dot{\theta}_{2x}, \dot{\theta}_{2z}]^T$, then the state space equation of the unit A_2 is

$$\dot{\boldsymbol{u}}_{A2} = \boldsymbol{\Lambda}_0\cdot\boldsymbol{u}_{A2} + \boldsymbol{f}_{A2}(\boldsymbol{F}_2) + \boldsymbol{f}_{in2}(t) \quad (2)$$

where $\boldsymbol{F}_2 = [F_{A5}, F_{A6}, F_{A7}, F_{A8}]^T$ is an excitation force column vector of the unit A_2 to its four supports; $\boldsymbol{f}_{A2}(\boldsymbol{F}_2) = [0, 0, 0, -\boldsymbol{I}_{1\times4}\cdot\boldsymbol{F}_2/m_2, \boldsymbol{Z}_2\cdot\boldsymbol{F}_2/J_{2x}, -\boldsymbol{X}_2\cdot\boldsymbol{F}_2/J_{2z}]^T$ denotes a vector function with respect to $\boldsymbol{F}_2$; $\boldsymbol{f}_{in2} = [0, 0, 0, F_2/m_2, 0, T_2/J_{2z}]^T$ is a known external input vector function; m_2, J_{2x}, and J_{2z} are the mass of the unit A_2 and the moment of inertia that bypasses its centroid and is parallel to the axis of Ox and Oz, respectively; $\boldsymbol{X}_2 = [0.5h_{2x}, 0.5h_{2x}, -0.5h_{2x}, -0.5h_{2x}]$; $\boldsymbol{Z}_2 = [-0.5h_{2z}, 0.5h_{2z}, -0.5h_{2z}, 0.5h_{2z}]$.

Combining the units A_1 and A_2 into the vibration source equipment subsystem, Equations (1) and (2) are merged into the following state space equation:

$$\dot{\boldsymbol{u}}_{\mathrm{A}}=\begin{bmatrix}\dot{\boldsymbol{u}}_{\mathrm{A1}}\\ \dot{\boldsymbol{u}}_{\mathrm{A2}}\end{bmatrix}=\begin{bmatrix}\boldsymbol{\Lambda}_0 & \boldsymbol{O}_{6\times6}\\ \boldsymbol{O}_{6\times6} & \boldsymbol{\Lambda}_0\end{bmatrix}\begin{bmatrix}\boldsymbol{u}_{\mathrm{A1}}\\ \boldsymbol{u}_{\mathrm{A2}}\end{bmatrix}+\begin{bmatrix}\boldsymbol{f}_{\mathrm{A1}}(\boldsymbol{F}_1)\\ \boldsymbol{f}_{\mathrm{A2}}(\boldsymbol{F}_2)\end{bmatrix}+\begin{bmatrix}\boldsymbol{f}_{\mathrm{in1}}(t)\\ \boldsymbol{f}_{\mathrm{in2}}(t)\end{bmatrix}=\boldsymbol{\Lambda}\cdot\boldsymbol{u}_{\mathrm{A}}+\boldsymbol{f}_{\mathrm{A}}(\boldsymbol{F}_1,\boldsymbol{F}_2)+\boldsymbol{f}_{\mathrm{in}}(t) \tag{3}$$

For the raft frame **R**, its vertical vibration displacement is represented by y_{R}; its angular displacement around the Ox axis is represented by $\theta_{\mathrm{R}x}$; and its angular displacement around the Oy axis is represented by $\theta_{\mathrm{R}y}$. Define a state variable $\boldsymbol{u}_{\mathrm{R}}=[u_{\mathrm{R1}},u_{\mathrm{R2}},u_{\mathrm{R3}},u_{\mathrm{R4}},u_{\mathrm{R5}},u_{\mathrm{R6}}]^{\mathrm{T}}=[y_{\mathrm{R}},\theta_{\mathrm{R}x},\theta_{\mathrm{R}z},\dot{y}_{\mathrm{R}},\dot{\theta}_{\mathrm{R}x},\dot{\theta}_{\mathrm{R}z}]^{\mathrm{T}}$, then the state space equation of the raft frame **R** is

$$\dot{\boldsymbol{u}}_{\mathrm{R}}=\begin{bmatrix}\dot{u}_{\mathrm{R1}}\\ \dot{u}_{\mathrm{R2}}\\ \dot{u}_{\mathrm{R3}}\\ \dot{u}_{\mathrm{R4}}\\ \dot{u}_{\mathrm{R5}}\\ \dot{u}_{\mathrm{R6}}\end{bmatrix}=\begin{bmatrix}0&0&0&1&0&0\\ 0&0&0&0&1&0\\ 0&0&0&0&0&1\\ 0&0&0&0&0&0\\ 0&0&0&0&0&0\\ 0&0&0&0&0&0\end{bmatrix}\begin{bmatrix}u_{\mathrm{R1}}\\ u_{\mathrm{R2}}\\ u_{\mathrm{R3}}\\ u_{\mathrm{R4}}\\ u_{\mathrm{R5}}\\ u_{\mathrm{R6}}\end{bmatrix}+\begin{bmatrix}0\\ 0\\ 0\\ \boldsymbol{I}_{1\times8}\cdot(\boldsymbol{F}_{\mathrm{t}}-\boldsymbol{F}_{\mathrm{b}})/m_{\mathrm{R}}\\ (\boldsymbol{Z}_{\mathrm{R2}}\cdot\boldsymbol{F}_{\mathrm{b}}-\boldsymbol{Z}_{\mathrm{R1}}\cdot\boldsymbol{F}_{\mathrm{t}})/J_{\mathrm{R}x}\\ (\boldsymbol{X}_{\mathrm{R1}}\cdot\boldsymbol{F}_{\mathrm{t}}-\boldsymbol{X}_{\mathrm{R2}}\cdot\boldsymbol{F}_{\mathrm{b}})/J_{\mathrm{R}z}\end{bmatrix}=\boldsymbol{\Lambda}_0\cdot\boldsymbol{u}_{\mathrm{R}}+\boldsymbol{f}_{\mathrm{R}}(\boldsymbol{F}_{\mathrm{t}},\boldsymbol{F}_{\mathrm{b}}) \tag{4}$$

where $\boldsymbol{F}_{\mathrm{t}}=[F_{\mathrm{t1}},F_{\mathrm{t2}},F_{\mathrm{t3}},F_{\mathrm{t4}},F_{\mathrm{t5}},F_{\mathrm{t6}},F_{\mathrm{t7}},F_{\mathrm{t8}}]^{\mathrm{T}}$ and $\boldsymbol{F}_{\mathrm{b}}=[F_{\mathrm{b1}},F_{\mathrm{b2}},F_{\mathrm{b3}},F_{\mathrm{b4}}]^{\mathrm{T}}$ are excitation force column vectors of the upper supports to the raft frame and the raft frame to the lower supports, respectively; m_{R}, $J_{\mathrm{R}x}$, and $J_{\mathrm{R}z}$ are the mass of the raft frame and the moment of inertia that bypasses its centroid and is parallel to the axis of Ox and Oz, respectively; $\boldsymbol{X}_{\mathrm{R1}}=[0.5h_{1x},0.5h_{1x},-0.5h_{1x},-0.5h_{1x},0.5h_{2x},0.5h_{2x},-0.5h_{2x},-0.5h_{2x}]$; $\boldsymbol{X}_{\mathrm{R2}}=[0.5H_x,0.5H_x,-0.5H_x,-0.5H_x]$; $\boldsymbol{Z}_{\mathrm{R1}}=[-b_1-0.5h_{1z},-b_1+0.5h_{1z},-b_1-0.5h_{1z},-b_1+0.5h_{1z},b_2-0.5h_{2z},b_2+0.5h_{2z},b_2-0.5h_{2z},b_2+0.5h_{2z}]$; $\boldsymbol{Z}_{\mathrm{R2}}=[-0.5H_z,0.5H_z,-0.5H_z,0.5H_z]$; $\boldsymbol{f}_{\mathrm{R}}(\boldsymbol{F}_{\mathrm{t}},\boldsymbol{F}_{\mathrm{b}})$ denotes a vector function about $\boldsymbol{F}_{\mathrm{t}}$, $\boldsymbol{F}_{\mathrm{b}}$.

For the connection supports between the vibration source equipment and the raft frame, ignoring the effect of their mass, the power/response transfer relation is

$$F_{\mathrm{t}i}=F_{\mathrm{A}i}=f_i(\delta_i,\dot{\delta}_i),\ (i=1,2,\ldots,8) \tag{5}$$

where $\delta_i=w_{\mathrm{A}i}-w_{\mathrm{t}i}$, and there are linear relationships between $w_{\mathrm{A}i}$, $w_{\mathrm{t}i}$ and the state variables $\boldsymbol{u}_{\mathrm{A}}$ and $\boldsymbol{u}_{\mathrm{R}}$:

$$\begin{cases}\boldsymbol{w}_{\mathrm{A1}}=u_1\boldsymbol{I}_{4\times1}-u_2\boldsymbol{Z}_1^{\mathrm{T}}+u_3\boldsymbol{X}_1^{\mathrm{T}}, & \dot{\boldsymbol{w}}_{\mathrm{A1}}=u_4\boldsymbol{I}_{4\times1}-u_5\boldsymbol{Z}_1^{\mathrm{T}}+u_6\boldsymbol{X}_1^{\mathrm{T}}\\ \boldsymbol{w}_{\mathrm{A2}}=u_7\boldsymbol{I}_{4\times1}-u_8\boldsymbol{Z}_2^{\mathrm{T}}+u_9\boldsymbol{X}_2^{\mathrm{T}}, & \dot{\boldsymbol{w}}_{\mathrm{A2}}=u_{10}\boldsymbol{I}_{4\times1}-u_{11}\boldsymbol{Z}_2^{\mathrm{T}}+u_{12}\boldsymbol{X}_2^{\mathrm{T}}\\ \boldsymbol{w}_{\mathrm{t}}=u_{\mathrm{R1}}\boldsymbol{I}_{8\times1}-u_{\mathrm{R2}}\boldsymbol{Z}_{\mathrm{R1}}^{\mathrm{T}}+u_{\mathrm{R3}}\boldsymbol{X}_{\mathrm{R1}}^{\mathrm{T}}, & \dot{\boldsymbol{w}}_{\mathrm{t}}=u_{\mathrm{R4}}\boldsymbol{I}_{8\times1}-u_{\mathrm{R5}}\boldsymbol{Z}_{\mathrm{R1}}^{\mathrm{T}}+u_{\mathrm{R6}}\boldsymbol{X}_{\mathrm{R1}}^{\mathrm{T}}\end{cases} \tag{6}$$

where $\boldsymbol{w}_{\mathrm{A1}}=[w_{\mathrm{A1}},w_{\mathrm{A2}},w_{\mathrm{A3}},w_{\mathrm{A4}}]^{\mathrm{T}}$; $\boldsymbol{w}_{\mathrm{A2}}=[w_{\mathrm{A5}},w_{\mathrm{A6}},w_{\mathrm{A7}},w_{\mathrm{A8}}]^{\mathrm{T}}$; $\boldsymbol{w}_{\mathrm{t}}=[w_{\mathrm{t1}},w_{\mathrm{t2}},w_{\mathrm{t3}},w_{\mathrm{t4}},w_{\mathrm{t5}},w_{\mathrm{t6}},w_{\mathrm{t7}},w_{\mathrm{t8}}]^{\mathrm{T}}$.

Let $\boldsymbol{w}_{\mathrm{A}}=[\boldsymbol{w}_{\mathrm{A1}}{}^{\mathrm{T}},\boldsymbol{w}_{\mathrm{A2}}{}^{\mathrm{T}}]^{\mathrm{T}}$, then Equation (5) is expressed as:

$$\boldsymbol{F}_{\mathrm{A}}=\begin{bmatrix}\boldsymbol{F}_1\\ \boldsymbol{F}_2\end{bmatrix}=\boldsymbol{F}_{\mathrm{t}}=\boldsymbol{f}\big(\boldsymbol{w}_{\mathrm{A}}(\boldsymbol{u}_{\mathrm{A}})-\boldsymbol{w}_{\mathrm{t}}(\boldsymbol{u}_{\mathrm{R}}),\dot{\boldsymbol{w}}_{\mathrm{A}}(\boldsymbol{u}_{\mathrm{A}})-\dot{\boldsymbol{w}}_{\mathrm{t}}(\boldsymbol{u}_{\mathrm{R}})\big)=\bar{\boldsymbol{f}}(\boldsymbol{u}_{\mathrm{A}},\boldsymbol{u}_{\mathrm{R}}) \tag{7}$$

Similarly, for the connection supports between the raft frame and the cylindrical shell, ignoring the effect of their mass, the power/response transfer relation is

$$F_{\mathrm{b}j}=F_{\mathrm{y}j}=g_j(\kappa_j,\dot{\kappa}_j),\ (j=1,2,3,4) \tag{8}$$

where $\kappa_j=w_{\mathrm{b}j}-w_{\mathrm{y}j}$ and there is a linear relationship between $w_{\mathrm{b}j}$ and the state variable $\boldsymbol{u}_{\mathrm{R}}$:

$$\boldsymbol{w}_{\mathrm{b}}=u_{\mathrm{R1}}\boldsymbol{I}_{4\times1}-u_{\mathrm{R2}}\boldsymbol{Z}_{\mathrm{R2}}^{T}+u_{\mathrm{R3}}\boldsymbol{X}_{\mathrm{R2}}^{\mathrm{T}},\quad\dot{\boldsymbol{w}}_{\mathrm{b}}=u_{\mathrm{R4}}\boldsymbol{I}_{4\times1}-u_{\mathrm{R5}}\boldsymbol{Z}_{\mathrm{R2}}^{T}+u_{\mathrm{R6}}\boldsymbol{X}_{\mathrm{R2}}^{\mathrm{T}} \tag{9}$$

where $\boldsymbol{w}_{\mathrm{b}}=[w_{\mathrm{b1}},w_{\mathrm{b2}},w_{\mathrm{b3}},w_{\mathrm{b4}}]^{\mathrm{T}}$.

The cylindrical shell is a continuum, and its modal parameters of all orders can be solved analytically. Further, a state space equation is established by using the modal parameters. The above is a common method for dealing with continuum problems. However, the cylindrical shell coupled with the external underwater acoustic field becomes a dissipative

system, so it is difficult to obtain an analytical expression of the modal parameters through theoretical deduction. In view of the above problem, a discrete numerical solution of displacement admittance functions is first calculated for the cylindrical shell—underwater acoustic field coupled subsystem by referring to Equations (11)–(18) in the literature [33]. Then, analytical expressions are fitted according to the admittance functions data, and then system modal parameters are identified from the expressions. Finally, a state space equation is established by using these modal parameters.

For the modal parameter identification method and modeling process mentioned above, please refer to Appendix A. Here, the state space equation after modeling is directly given for the cylindrical shell—underwater acoustic field coupled subsystem:

$$\dot{\boldsymbol{u}}_{\mathrm{C}} = \boldsymbol{S}_{\mathrm{C}}\boldsymbol{u}_{\mathrm{C}} + \overline{\boldsymbol{\Phi}}_{\mathrm{C}}\boldsymbol{F}_{\mathrm{y}} \tag{10}$$

where $\boldsymbol{u}_{\mathrm{C}} = [u_{\mathrm{C1}}, u_{\mathrm{C2}}, u_{\mathrm{C3}}, \ldots, u_{\mathrm{C}f}]^{\mathrm{T}}$ is a state variable (f is first f-order modes intercepted for the low-frequency vibration problem); $\boldsymbol{F}_{\mathrm{y}} = [F_{\mathrm{y1}}, F_{\mathrm{y2}}, F_{\mathrm{y3}}, F_{\mathrm{y4}}]^{\mathrm{T}}$ is an excitation force column vector of the connection supports to the cylindrical shell; $\boldsymbol{S}_{\mathrm{C}} = \mathrm{diag}[s_{\mathrm{C1}}, s_{\mathrm{C2}}, s_{\mathrm{C3}}, \ldots, s_{\mathrm{C}f}]$ is a diagonal matrix composed of poles $s_{\mathrm{C}i}$ obtained by modal parameter identification ($s_{\mathrm{C}i}$ sorted by $|s_{\mathrm{C1}}| < |s_{\mathrm{C2}}| < |s_{\mathrm{C3}}| < \ldots < |s_{\mathrm{C}f}|$); $\overline{\boldsymbol{\Phi}}_{\mathrm{C}}$ is a matrix composed of identified modal parameter $\overline{\phi}_{ij}$ (i = 1, 2, …, f is modal order; j = 1, 2, 3, 4 is the position of the connection point between the lower support and the cylindrical shell), and

$$\overline{\boldsymbol{\Phi}}_{\mathrm{C}} = \begin{bmatrix} \overline{\phi}_{11} & \overline{\phi}_{12} & \overline{\phi}_{13} & \overline{\phi}_{14} \\ \overline{\phi}_{21} & \overline{\phi}_{22} & \overline{\phi}_{23} & \overline{\phi}_{24} \\ \overline{\phi}_{31} & \overline{\phi}_{32} & \overline{\phi}_{33} & \overline{\phi}_{34} \\ \vdots & \vdots & \vdots & \vdots \\ \overline{\phi}_{f1} & \overline{\phi}_{f2} & \overline{\phi}_{f3} & \overline{\phi}_{f4} \end{bmatrix} \tag{11}$$

The functional relation between $w_{\mathrm{y}j}$ and the state space variable $\boldsymbol{u}_{\mathrm{C}}$ is

$$\boldsymbol{w}_{\mathrm{y}} = 2\mathrm{Re}\left\{\overline{\boldsymbol{\Phi}}_{\mathrm{C}}^{\mathrm{T}}\boldsymbol{u}_{\mathrm{C}}\right\} = 2\left(\mathrm{Re}\left\{\overline{\boldsymbol{\Phi}}_{\mathrm{C}}^{T}\right\}\cdot\mathrm{Re}\{\boldsymbol{u}_{\mathrm{C}}\} - \mathrm{Im}\left\{\overline{\boldsymbol{\Phi}}_{\mathrm{C}}^{T}\right\}\cdot\mathrm{Im}\{\boldsymbol{u}_{\mathrm{C}}\}\right) \tag{12}$$

where $\boldsymbol{w}_{\mathrm{y}} = [w_{\mathrm{y1}}, w_{\mathrm{y2}}, w_{\mathrm{y3}}, w_{\mathrm{y4}}]^{\mathrm{T}}$.

By combining the state space equations (Equations (3), (4), and (10)) of the vibration source equipment, raft frame, and cylindrical shell into one, the total state space equation of the system is formed. Then, through the constitutive equation of the elastic elements (Equations (5) and (8)), the subsystems can be connected into a whole.

2.3. Expression of Nonlinear Stiffness for Vibration Isolation Supports

In Equations (5) and (8), the constitutive relation of the elastic supports is only expressed in general terms, which can be a linear or nonlinear function. For the nonlinear stiffness characteristics of vibration isolation supports, they are generally classified qualitatively into two categories: softening and hardening characteristics, as shown in Figure 2a,b. The blue curve in Figure 2 indicates the nonlinear stiffness characteristics expressed by a piecewise linear method, where δ_0 is an approximate linear stiffness working interval control parameter, and K_1 and K_2 are approximate stiffness control parameters inside and outside the linear working interval, respectively. In practical problems, the transition from linear to nonlinear generally has a gradual process, rather than a sudden change, and the piecewise curve is not easy to deal with in numerical calculation because of its unsmoothness. So, the piecewise turning function is modified to a smooth transition function, as shown by the red curve in Figure 2.

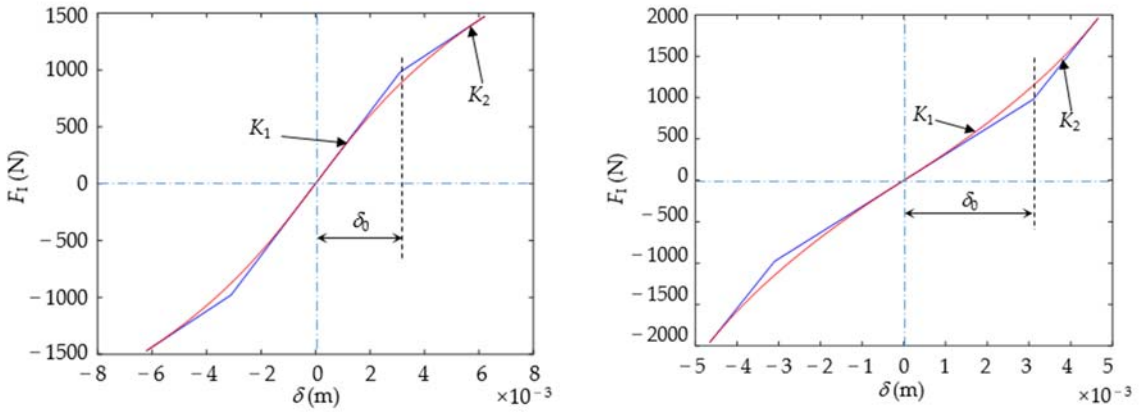

(**a**) (**b**)

Figure 2. Nonlinear stiffness characteristics and their control parameters: (**a**) softening characteristic; (**b**) hardening characteristic.

The softening and hardening characteristics are expressed in this paper as Equations (13) and (14), respectively:

$$\begin{cases} \delta = \dfrac{|\tau| + K_1 c_1 \left[\sqrt[3]{1+(\tau/c_2)^3} - 1\right]}{\sqrt{1+K_1^2}} \mathrm{sgn}(\tau), \quad F_I = \dfrac{K_1|\tau| - c_1 \left[\sqrt[3]{1+(\tau/c_2)^3} - 1\right]}{\sqrt{1+K_1^2}} \mathrm{sgn}(\tau) \\ c_1 = \frac{K_1 - K_2}{1+K_1 K_2} c_2, c_2 = \sqrt{1+K_1^2}\delta_0, \quad \tau = |\tau|\mathrm{sgn}(\delta) \\ \left[(K_1 c_1/c_2)^3 + 1\right]|\tau|^3 - 3\left(\sqrt{1+K_1^2}|\delta| + K_1 c_1\right)|\tau|^2 + 3\left(\sqrt{1+K_1^2}|\delta| + K_1 c_1\right)^2|\tau| - \left(\sqrt{1+K_1^2}|\delta| + K_1 c_1\right)^3 + (K_1 c_1)^3 = 0 \end{cases} \tag{13}$$

where $\mathrm{sgn}(\tau)$ is the sign function; c_1 and c_2 are shape control parameters determined by K_1, K_2, and δ_0; τ is a parameter variable related to the positive real root $|\tau|$ of the polynomial equation.

$$\begin{cases} \delta = \dfrac{|\tau| - K_1 c_1 \left[\sqrt[3]{1+(\tau/c_2)^3} - 1\right]}{\sqrt{1+K_1^2}} \mathrm{sgn}(\tau), \quad F_I = \dfrac{K_1|\tau| + c_1 \left[\sqrt[3]{1+(\tau/c_2)^3} - 1\right]}{\sqrt{1+K_1^2}} \mathrm{sgn}(\tau) \\ c_1 = \frac{K_2 - K_1}{1+K_1 K_2} c_2, c_2 = \sqrt{1+K_1^2}\delta_0, \quad \tau = |\tau|\mathrm{sgn}(\delta) \\ \left[(K_1 c_1/c_2)^3 - 1\right]|\tau|^3 + 3\left(\sqrt{1+K_1^2}|\delta| - K_1 c_1\right)|\tau|^2 - 3\left(\sqrt{1+K_1^2}|\delta| - K_1 c_1\right)^2|\tau| + \left(\sqrt{1+K_1^2}|\delta| - K_1 c_1\right)^3 + (K_1 c_1)^3 = 0 \end{cases} \tag{14}$$

It is assumed that the three groups of vibration isolation supports have the same constitutive relation under the unit A_1, the unit A_2, and the floating raft R. The K_1 of the three groups of vibration isolators are denoted as $K_{A11} = \mathrm{Re}\{k_1\}$, $K_{A21} = \mathrm{Re}\{k_2\}$, and $K_{R1} = \mathrm{Re}\{k_R\}$, respectively, where k_1, k_2, and k_R are the linear complex stiffness. The K_2 of the three groups of isolators (denoted as K_{A12}, K_{A22}, and K_{R2}, respectively) is set as α (stiffness ratio) times K_1, that is, $K_{A12} = \alpha K_{A11}$, $K_{A22} = \alpha K_{A21}$, and $K_{R2} = \alpha K_{R1}$, where $\alpha \in [0.1, 3.0]$ (softening characteristic when $\alpha < 1.0$ and hardening characteristic when $\alpha > 1.0$). The δ_0 (denoted as δ_{10}, δ_{20}, and δ_{R0}, respectively) of the three groups of isolators is estimated to be β times their respective static settlement after installation of the units, that is, $\delta_{10} = \beta m_1 g/\mathrm{Re}\{4k_1\}$, $\delta_{20} = \beta m_2 g/\mathrm{Re}\{4k_2\}$, and $\delta_{R0} = \beta(m_1 + m_2 + m_R)g/\mathrm{Re}\{4k_R\}$, where $\beta \in [0.2, 5.0]$. In addition, the structural damping coefficients of the vibration isolators are approximately converted to the equivalent viscous damping coefficients by $c_1 = \mathrm{Im}\{k_1\}/\omega_1$, $c_2 = \mathrm{Im}\{k_2\}/\omega_1$, and $c_R = \mathrm{Im}\{k_R\}/\omega_1$ (where ω_1 is the fundamental frequency of the system).

2.4. Evaluation Index of Vibro-Acoustic Transfer Characteristics for the Nonlinear Coupled System

The transmitted power flow (which refers to the vibrational power flow transferred to the cylindrical shell through the supports under the floating raft in this paper) can reflect the process of vibration energy transfer and conversion into underwater acoustic radiation

of the coupled system [34], which can be regarded as a comprehensive reflection of the vibro-acoustic transfer characteristics.

For the coupled system shown in Figure 1, the instantaneous power of the excitation $\boldsymbol{F}_{\mathrm{y}}$ acting on the cylindrical shell by the vibration isolation support is

$$I(t) = \boldsymbol{F}_{\mathrm{y}}^{T} \cdot \dot{\boldsymbol{w}}_{\mathrm{y}} \tag{15}$$

The vibrational power flow is the average power of the excitation over a period $T = 2\pi/\omega$:

$$P_T = \frac{1}{T}\int_0^T I(t)dt \tag{16}$$

Similar to this, the time average power is introduced:

$$\overline{I}(t) = \frac{1}{t}\int_0^t I(\tau)d\tau \tag{17}$$

The initial value $\overline{I}(t)$ can be obtained by the above equation.

$$\overline{I}(0) = \lim_{t\to 0}\frac{1}{t}\int_0^t I(\tau)d\tau = \lim_{t\to 0} I(t) = I(0) = 0 \tag{18}$$

The derivative of time t on both sides of Equation (17) is calculated:

$$\dot{\overline{I}}(t) = -\frac{1}{t^2}\int_0^t I(\tau)d\tau + \frac{I(t)}{t} = \frac{-\overline{I}(t) + I(t)}{t} \tag{19}$$

From the above equation, combined with Equations (3), (4), (10), and (15), the initial value $\dot{\overline{I}}(t)$ can be obtained:

$$\dot{\overline{I}}(0) = \frac{1}{2}\lim_{t\to 0}\left(\dot{\boldsymbol{F}}_{\mathrm{y}}^{T}\cdot\dot{\boldsymbol{w}}_{\mathrm{y}} + \boldsymbol{F}_{\mathrm{y}}^{T}\cdot\ddot{\boldsymbol{w}}_{\mathrm{y}}\right) = \frac{1}{2}\lim_{t\to 0}\left(\dot{\boldsymbol{F}}_{\mathrm{y}}^{T}\cdot 2\mathrm{Re}\left\{\boldsymbol{\Phi}_{\mathrm{C}}^{-\mathrm{T}}\boldsymbol{S}_{\mathrm{C}}\boldsymbol{u}_{\mathrm{C}}\right\} + \boldsymbol{g}^{T}\left(\boldsymbol{w}_{\mathrm{y}} - \boldsymbol{w}_{\mathrm{b}}, \dot{\boldsymbol{w}}_{\mathrm{y}} - \dot{\boldsymbol{w}}_{\mathrm{b}}\right)\cdot\ddot{\boldsymbol{w}}_{\mathrm{y}}\right) = 0 \tag{20}$$

where the initial values of the system state variables $\boldsymbol{u}_{\mathrm{A}}$, $\boldsymbol{u}_{\mathrm{R}}$, and $\boldsymbol{u}_{\mathrm{C}}$ have been set to be $\boldsymbol{0}$ (the system is in a static state).

On the other hand, assuming that the vibration enters the steady state after a certain time t_0 and has a period T, it can be seen from Equation (17) that for any natural number N, the following equation holds:

$$(t_0 + NT)\overline{I}(t_0 + NT) - t_0\overline{I}(t_0) = \int_{t_0}^{t_0+NT} I(\tau)d\tau = \int_0^{NT} I(\tau)d\tau = NTP_T \tag{21}$$

Therefore, the vibration power flow can be calculated by the time average power:

$$P_T = \overline{I}(t_0 + T) + \frac{t_0}{T}\left[\overline{I}(t_0 + T) - \overline{I}(t_0)\right] \tag{22}$$

If t_0 is large enough, the system still does not exhibit perfect periodic oscillation. But as long as there is a mathematical expectation in Equation (16), then Equation (22) still holds. At this time, T can be understood as some kind of virtual value related to the excitation period, and P_T still represents the average power level of the excitation. Then, Equation (22) is rewritten as:

$$P_{\mathrm{T}} = \left[(T + t_0)\overline{I}(t_0 + T) - t_0\overline{I}(t_0)\right]/T \tag{23}$$

3. Results and Discussion

Based on the theories in Section 2, the effect of the nonlinear stiffness control parameters of the vibration isolation supports on the low-frequency vibration modes and

vibro-acoustic transfer characteristics of the coupled system are analyzed by numerical simulation methods in the following.

To obtain sufficient amplitude for the system to fully demonstrate its nonlinear vibration characteristics, the amplitude of the excitation force applied to the units A_1 and A_2 is set to 500 N. The values of the variable stiffness isolators and system structural parameters involved in the numerical simulations are set as shown in Tables 1 and 2, and other control parameters are shown in Appendix B.

Table 1. Control parameter settings of variable stiffness vibration isolator.

Control Parameters	Symbols	Units	Values	Remarks
Stiffness control parameters in the approximate linear working interval	K_{A11} K_{A21} K_{R1}	N/m N/m N/m	2.0×10^5 2.7×10^5 8.6×10^5	
Stiffness control parameters outside the linear working interval	K_{A12} K_{A22} K_{R2}	N/m N/m N/m	$\alpha \cdot 2.0 \times 10^5$ $\alpha \cdot 2.7 \times 10^5$ $\alpha \cdot 8.6 \times 10^5$	$\alpha \in [0.1, 3.0]$ $\alpha < 1$, softening characteristic $\alpha > 1$, hardening characteristic
Linear working interval length control parameters	δ_{10} δ_{20} δ_{R0}	m m m	$\beta \cdot 6.125 \times 10^{-4}$ $\beta \cdot 6.352 \times 10^{-4}$ $\beta \cdot 6.267 \times 10^{-4}$	$\beta \in [0.2, 5.0]$
Damping coefficients	c_1 c_2 c_R	kg/s kg/s kg/s	159.155 214.859 684.366	

Table 2. System structure parameter settings.

System Structure Parameters		Symbols	Units	Values
Characteristic parameters of the cylindrical shell	Elastic modulus	E	N/m^2	2.1×10^{11}
	Density	ρ	kg/m^3	7.8×10^3
	Poisson's ratio	μ		0.28
	Dissipation factor	ξ		0.01
	Length, radius, thickness	L, a, d	m	2, 0.4, 0.02
Structure parameters of the units and the raft frame	Mass of the unit A_1	m_1	kg	50
	Mass of the unit A_2	m_2	kg	70
	Mass of the raft frame R	m_R	kg	100
	Moment of inertia of the unit A_1	J_{1x}, J_{1z}	$Kg \cdot m^2$	1, 0.5
	Moment of inertia of the unit A_2	J_{2x}, J_{2z}	$Kg \cdot m^2$	1.5, 1
	Moment of inertia of the raft frame R	J_{Rx}, J_{Rz}	$Kg \cdot m^2$	8.5, 2.5
Linear complex stiffness of the vibration isolation supports	Support stiffness of the unit A_1	k_1	N/m	$2.0 \times 10^5 \times (1 + 0.1\,j)$
	Support stiffness of the unit A_2	k_2	N/m	$2.7 \times 10^5 \times (1 + 0.1\,j)$
	Support stiffness of the raft frame R	k_R	N/m	$8.6 \times 10^5 \times (1 + 0.1\,j)$
Installation position parameters	Centroid positioning of the unit A_1	b_1	m	0.25
	Centroid positioning of the unit A_2	b_2	m	0.25
	Centroid positioning of the raft frame R	L_R	m	0.8
	Support spacing of the unit A_1	h_{1x}, h_{1z}	m	0.2, 0.3
	Support spacing of the unit A_2	h_{2x}, h_{2z}	m	0.2, 0.3
	Support spacing of the raft frame R	H_x, H_z	m	0.35, 0.7

3.1. Modal Parameter Identification for the Cylindrical Shell—Underwater Acoustic Field Coupled Subsystem

Taking the displacement derivative functions H_{11}, H_{12}, and H_{14} as examples, their fitting spectra obtained from the modal parameter identification method are compared with the numerical spectra obtained by the calculation method in the literature [33], as shown in Figure 3. It can be seen that the fitting results can match well with the original

data, and the difference between the two is mainly related to the modal truncation (residual admittance) and the computational error of the original data.

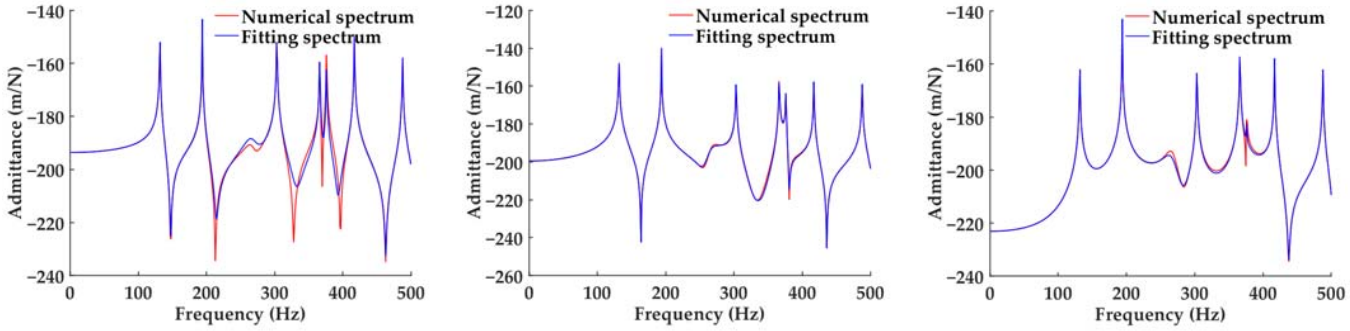

Figure 3. Comparison of the fitting spectra and the numerical spectra: (**a**) H_{11}; (**b**) H_{12}; (**c**) H_{14}.

The first 10 orders of poles identified for the cylindrical shell—underwater acoustic field coupled subsystem and their corresponding modal frequencies are listed in Table 3. The values of the modal parameters $\overline{\phi}_{ij}$ at the support connection points are listed in Table 4.

Table 3. The first 10 orders of poles and modal frequencies of the cylindrical shell—underwater acoustic field coupled subsystem.

Orders i	Poles s_{Ci}, s_{Ci}^{*} *	Modal Frequencies f_{Ci} (Hz)
1	$-0.366 \pm 8.277 \times 10^2$ j	131.73
2	$-0.574 \pm 1.219 \times 10^3$ j	194.95
3	$-0.660 \pm 1.672 \times 10^3$ j	266.24
4	$-0.924 \pm 1.906 \times 10^3$ j	303.33
5	$-1.246 \pm 2.302 \times 10^3$ j	366.30
6	$-1.753 \pm 2.364 \times 10^3$ j	376.21
7	$-1.307 \pm 2.621 \times 10^3$ j	417.11
8	$-1.586 \pm 3.065 \times 10^3$ j	487.86
9	$-3.624 \pm 3.304 \times 10^3$ j	525.88
10	$-2.863 \times 10^3 \pm 1.973 \times 10^3$ j	553.34

* The poles s_{Ci} and s_{Ci}^{*} are a pair of conjugate complex numbers.

Table 4. The values of the modal parameters $\overline{\phi}_{ij}$ at the support connection points.

Orders i	$j = 1$	$j = 2$	$j = 3$	$j = 4$
$i = 1$	0.475 − 4.630 j	0.686 − 0.703 j	0.104 − 0.117 j	0.163 − 0.172 j
$i = 2$	0.462 − 0.429 j	0.601 − 0.647 j	−0.317 + 0.312 j	−0.448 + 0.469 j
$i = 3$	0.436 − 0.208 j	0.271 − 0.328 j	0.068 − 0.226 j	0.214 − 0.335 j
$i = 4$	0.510 − 0.529 j	−0.274 + 0.240 j	−0.398 + 0.384 j	0.170 − 0.169 j
$i = 5$	0.367 − 0.352 j	0.402 − 0.441 j	−0.347 + 0.339 j	−0.453 + 0.479 j
$i = 6$	0.159 − 0.407 j	−0.342 + 0.117 j	0.412 − 0.031 j	0.006 + 0.032 j
$i = 7$	0.473 − 0.475 j	−0.218 + 0.218 j	−0.464 + 0.464 j	0.215 − 0.215 j
$i = 8$	0.357 − 0.356 j	−0.317 + 0.318 j	−0.261 + 0.261 j	0.233 − 0.234 j
$i = 9$	0.470 − 0.434 j	−0.254 + 0.271 j	−0.361 + 0.357 j	0.248 − 0.270 j
$i = 10$	0.716 − 0.762 j	0.082 − 0.105 j	−0.244 + 0.233 j	−0.053 + 0.012 j

3.2. Effect of Nonlinear Stiffness with Softening Characteristic on the Low-Frequency Vibro-Acoustic Characteristics for the Coupled System

3.2.1. Effect of Stiffness Ratio α

Figure 4 shows the bifurcation diagrams of the average vibration displacement and velocity for the coupled system when β is 1.0 and α is 1.0, 0.9, 0.7, 0.5, 0.3, and 0.1, respectively. Taking $\alpha = 0.1$ as an example, the discontinuity points near 6.75 Hz in the figure are

caused by the system resonating at the natural frequency, while the other discontinuity points are caused by the simulation program setting different steps in different frequency bands to improve the calculation efficiency. The discontinuity points in Figure 4 and in the bifurcation diagram below are the same and will not be explained one by one. It can be seen from Figure 4 that the steady vibration of the coupled system with nonlinear softening stiffness supports is single-periodic motion.

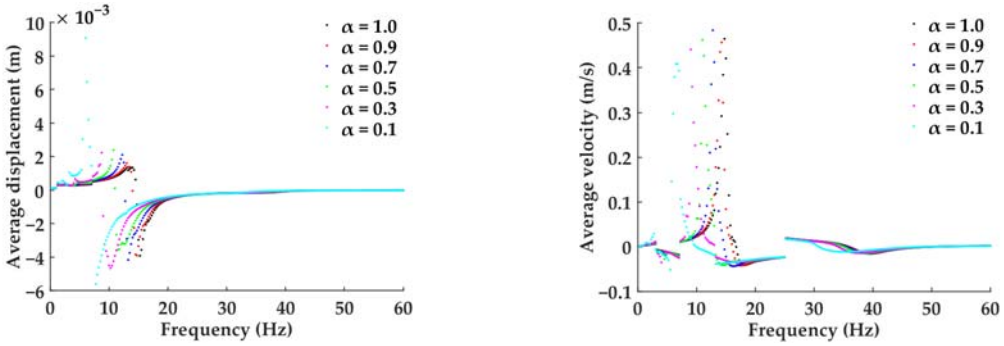

(**a**) (**b**)

Figure 4. Effect of the strength variation of the nonlinear softening stiffness characteristic on the periodic bifurcation properties for the coupled system (β = 1.0): (**a**) bifurcation diagram of the average vibration displacement; (**b**) bifurcation diagram of the average vibration velocity.

Figure 5 shows the motion phase diagrams of the coupled system corresponding to the resonance frequencies of Figure 4. According to Figure 5a–d, when the softening characteristic is weak (α = 0.9), the units A_1, A_2 and the raft frame all are presented as approximate harmonic vibration modes. As the stiffness ratio decreases, the motion phase diagrams gradually show irregular closed graphics, indicating that the motions of the units A_1, A_2 and the raft frame are still single-periodic, but there are superharmonic components. According to Figure 5e, the vibration form at the connection points of the lower vibration isolators with the cylindrical shell is much more complex than that of the units A_1, A_2 and the raft frame, and the smaller the α, the more complex the vibration form. When α is equal to 0.1, the motion phase diagrams have become disordered or even chaotic. It can also be seen from Figure 5 that in a certain range of stiffness ratio $\alpha < 1.0$, the resonance displacement amplitudes of the units A_1, A_2 and the raft frame are larger than those of α = 1.0 (linear stiffness), and the smaller the α, the larger the amplitudes. The resonance velocity amplitudes show the opposite trend. In contrast, at the connection points of the lower vibration isolators with the cylindrical shell, the amplitudes of both the resonance displacement and resonance velocity decrease with the decrease in α. But the above law no longer holds when α decreases to a certain extent, as shown in Figure 5e, which is broken when α is equal to 0.1.

In addition, it can be found from Figure 5 that, when the vibration isolation supports have softening stiffness characteristics, the motion laws at the connection points of the upper vibration isolators with units A_1 and A_2 are basically the same, and the motion laws at the connection points of the upper and lower vibration isolators with the raft frame are also basically similar. In fact, through the simulation analysis, it can be seen that the above laws are also established when the vibration isolation supports have hardening stiffness characteristics. Therefore, in the following, only the motion phase diagrams are shown and analyzed at the connection points of the upper vibration isolators with the unit A_1, the lower vibration isolators with the raft frame, and the lower vibration isolators with the cylindrical shell.

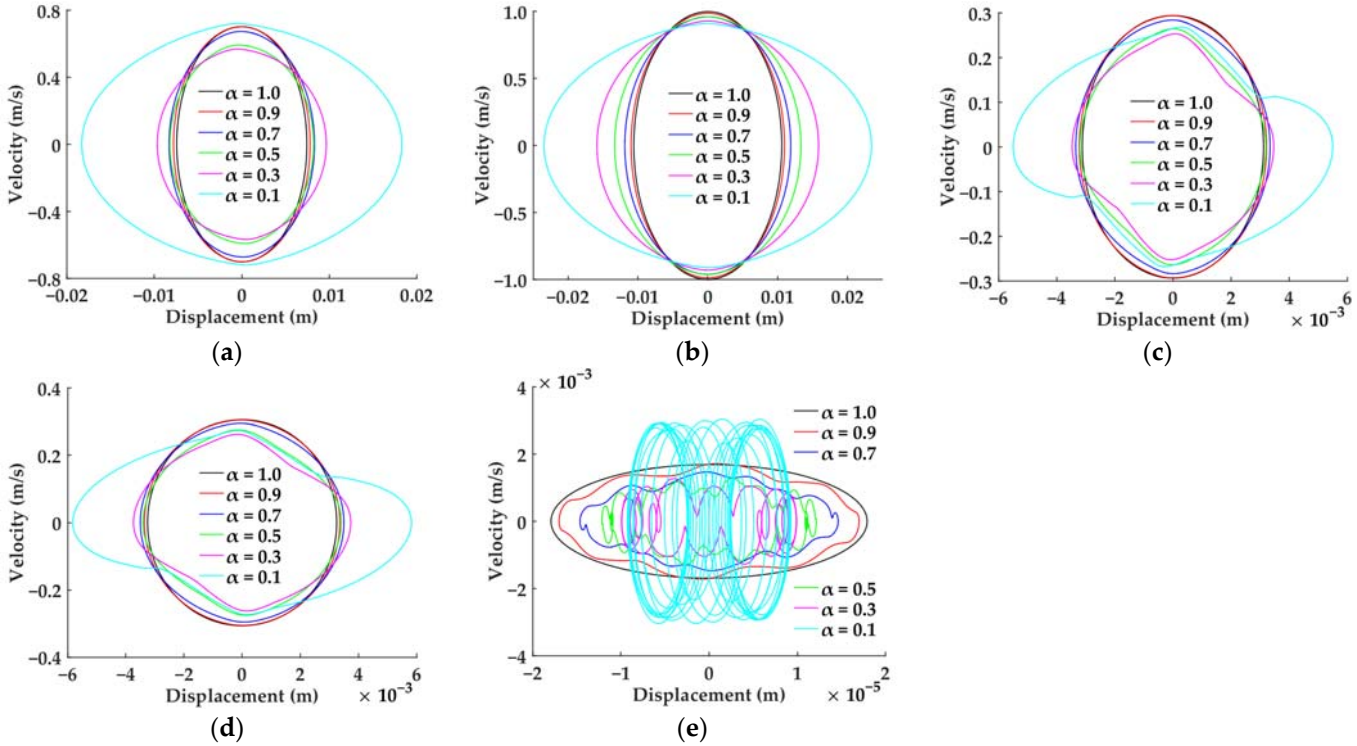

Figure 5. Effect of the strength variation of the nonlinear softening stiffness characteristic on the low-frequency vibration modes for the coupled system (β = 1.0): (**a**) motion phase diagram at the connection points of the upper vibration isolators with the unit A_1; (**b**) motion phase diagram at the connection points of the upper vibration isolators with the unit A_2; (**c**) motion phase diagram at the connection points of the upper vibration isolators with the raft frame; (**d**) motion phase diagram at the connection points of the lower vibration isolators with the raft frame; (**e**) motion phase diagram at the connection points of the lower vibration isolators with the cylindrical shell.

Figure 6 shows the transmitted power flow spectrum through the lower vibration isolators input to the cylindrical shell in the coupled system when β is 1.0 and α is 1.0, 0.9, 0.7, 0.5, 0.3, and 0.1, respectively. As can be seen from Figure 6, compared to the linear stiffness, the softening nonlinear characteristic of the support stiffness makes the resonance region of the system shift to lower frequencies, and the resonance peak and the second peak decrease. The smaller α is, the more significant the above effect is.

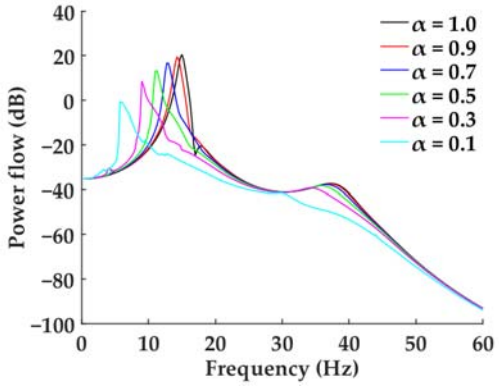

Figure 6. Effect of the strength variation of the nonlinear softening stiffness characteristic on the vibro-acoustic transfer characteristics for the coupled system (β = 1.0).

3.2.2. Effect of Approximate Linear Working Interval Length Control Parameter β

Figure 7 shows the bifurcation diagrams of the average vibration displacement and velocity for the coupled system when α is 0.5 and β is 5.0, 3.0, 2.0, 1.0, and 0.2, respectively. Comparing Figure 7 with Figure 4, it can be seen that the two are quite similar, and the steady state vibration of the coupled system is still single-periodic motion.

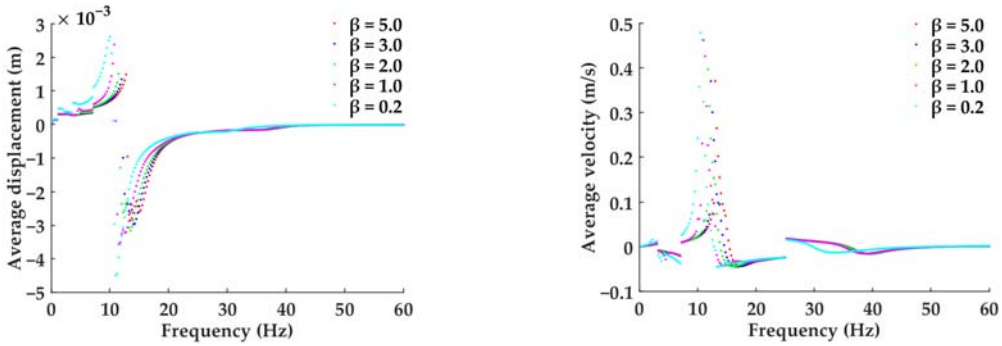

Figure 7. Effect of the length variation of the approximate linear working interval on the periodic bifurcation properties for the coupled system (α = 0.5): (**a**) bifurcation diagram of the average vibration displacement; (**b**) bifurcation diagram of the average vibration velocity.

Figure 8 shows the motion phase diagrams of the coupled system corresponding to the resonance frequencies of Figure 7. Since the stiffness ratio α = 0.5 here has determined that the vibration isolation supports have softening stiffness characteristics, reducing the approximate linear working interval will further strengthen their nonlinear stiffness characteristics. The results are that the amplitudes of the resonance displacement and resonance velocity of the unit, the raft frame, and the connection points of the lower vibration isolators with the cylindrical shell generally tend to increase with the decrease in β. From the perspective of motion form, the motion phase diagram of the unit is approximately a closed ellipse, that is, it is approximately a harmonic vibration. The motion phase diagram of the raft frame is irregular and closed, indicating that it contains strong superharmonic components. The motion phase diagram at the connection points of the lower vibration isolators with the cylindrical shell is relatively complex, indicating that the superharmonic components are complex and strong, and the phase diagram trajectory tends to be messy or even chaotic due to the enhancement of the nonlinear softening characteristic.

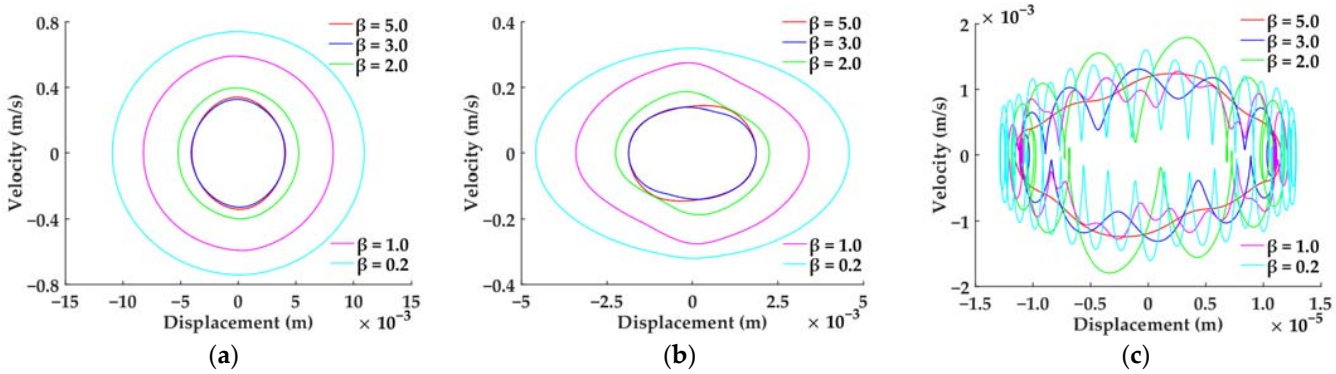

Figure 8. Effect of the length variation of the approximate linear working interval on the low-frequency vibration modes for the coupled system (α = 0.5): (**a**) motion phase diagram at the connection points of the upper vibration isolators with the unit A_1; (**b**) motion phase diagram at the connection points of the lower vibration isolators with the raft frame; (**c**) motion phase diagram at the connection points of the lower vibration isolators with the cylindrical shell.

Figure 9 shows the transmitted power flow spectrum in the coupled system when α is 0.5 and β is 5.0, 3.0, 2.0, 1.0, and 0.2, respectively. Comparing Figure 9 with Figure 6, it can be seen that the effect of reducing β is similar to that of reducing α. Both of them enhance the nonlinear softening stiffness effect and make the resonance region move to the lower frequency for the coupled system. Reducing α has a more obvious effect on reducing the fundamental frequency of the system and also weakens the resonance sharpness. But reducing β is more effective for reducing the transmitted power flow at higher frequencies after the fundamental frequency. For example, when α is equal to 0.5 and β is equal to 0.2 in Figure 9, the transmitted power flow level is significantly reduced on the band after the fundamental frequency and, especially, the second peak tends to disappear.

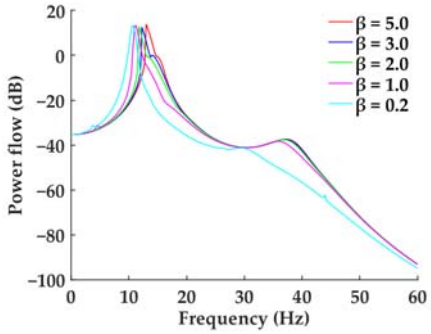

Figure 9. Effect of the length variation of the approximate linear working interval on the vibro-acoustic transfer characteristics for the coupled system (α = 0.5).

3.3. Effect of Nonlinear Stiffness with Hardening Characteristic on the Low-Frequency Vibro-Acoustic Characteristics for the Coupled System

3.3.1. Effect of Stiffness Ratio α

Figure 10 shows the bifurcation diagrams of the average vibration displacement and velocity for the coupled system when β is 1 and α is 1.0, 1.2, 1.5, 2.0, 2.5, and 3.0, respectively. It can be seen that the steady vibration of the coupled system with nonlinear hardening stiffness supports is dominated by single-periodic motion, but when the nonlinear hardening characteristic is enhanced (α = 2.0, 2.5, 3.0), aperiodic motion (quasi-periodic or chaotic) appears in a frequency band after the fundamental frequency resonance region.

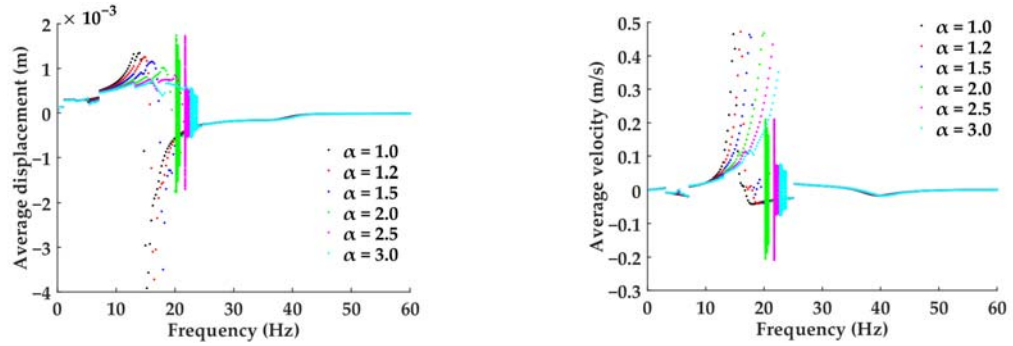

(**a**) (**b**)

Figure 10. Effect of the strength variation of the nonlinear hardening stiffness characteristic on the periodic bifurcation properties for the coupled system (β = 1.0): (**a**) bifurcation diagram of the average vibration displacement; (**b**) bifurcation diagram of the average vibration velocity.

Figure 11 shows the motion phase diagrams of the coupled system corresponding to the resonance frequencies of Figure 10. According to Figure 11a, when the hardening characteristic is weak (α = 1.2, 1.5, 2.0), the unit is presented as an approximate harmonic vibration mode. But as the stiffness ratio further increases (α = 2.5, 3.0), the motion phase diagrams gradually become nonelliptical closed graphics, indicating that the motion of

the unit is still single-periodic, but there are superharmonic components. According to Figure 5b,c, the motion phase diagrams of the raft and the connection points of the lower vibration isolators with the cylindrical shell are all irregular closed graphics, indicating that their vibration modes are all single-period motion with superharmonics, and the vibration form at the connection points of the lower vibration isolators with the cylindrical shell is particularly complex. Through the calculation and analysis at different frequencies, it can be found that the above vibration modes and laws are universal in the coupled system with hardening characteristic stiffness supports. It can also be seen from Figure 11 that, when stiffness ratio $\alpha > 1.0$, the resonance displacement amplitudes of the unit and the raft frame are smaller than those of $\alpha = 1.0$ (linear stiffness), and the larger the α, the smaller the amplitudes. The resonance velocity amplitudes have no consistent change rule. In contrast, at the connection points of the lower vibration isolators with the cylindrical shell, the amplitudes of both the resonance displacement and resonance velocity increase with the increase in α. But they do not conform when α is equal to 3.0, indicating that the above law only holds in a certain range of $\alpha > 1.0$.

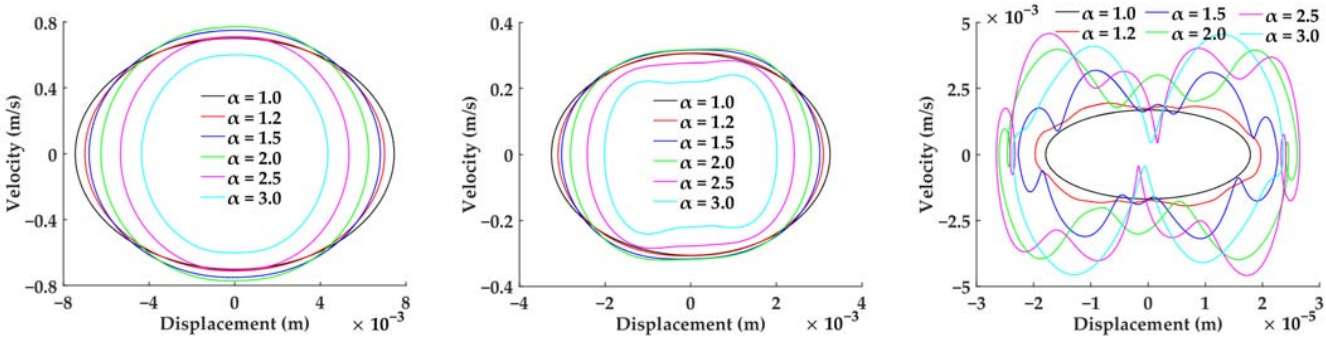

Figure 11. Effect of the strength variation of the nonlinear hardening stiffness characteristic on the low-frequency vibration modes for the coupled system ($\beta = 1.0$): (**a**) motion phase diagram at the connection points of the upper vibration isolators with the unit A_1; (**b**) motion phase diagram at the connection points of the lower vibration isolators with the raft frame; (**c**) motion phase diagram at the connection points of the lower vibration isolators with the cylindrical shell.

Figure 12 shows the transmitted power flow spectrum in the coupled system when β is 1.0 and α is 1.0, 1.2, 1.5, 2.0, 2.5, and 3.0, respectively. Comparing Figure 12 with Figure 6, it can be seen that the hardening and softening characteristics of the support stiffness have a significantly opposite effect on the transmitted power flow of the coupled system. The hardening nonlinear characteristic of the support stiffness makes the resonance region of the system shift to higher frequencies, and the resonance peak and the second peak increase slightly. The larger α is, the more significant the above effect is.

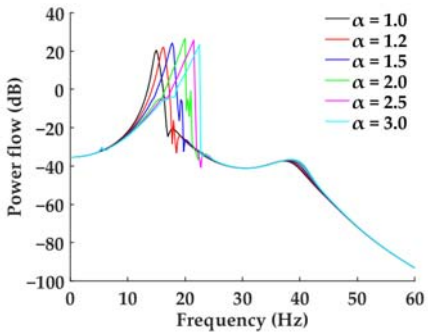

Figure 12. Effect of the strength variation of the nonlinear hardening stiffness characteristic on the vibro-acoustic transfer characteristics for the coupled system ($\beta = 1.0$).

3.3.2. Effect of Approximate Linear Working Interval Length Control Parameter β

Figure 13 shows the bifurcation diagrams of the average vibration displacement and velocity for the coupled system when α is 1.5 and β is 5.0, 3.0, 2.0, 1.0, and 0.2, respectively. Comparing Figure 13 with Figure 10, it can be seen that the two are quite similar, and the steady state vibration of the coupled system is always single-periodic motion when α is equal to 1.5.

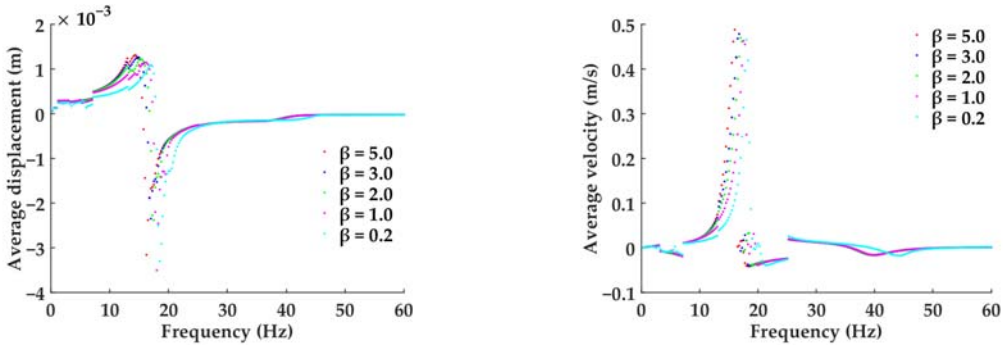

Figure 13. Effect of the length variation of the approximate linear working interval on the periodic bifurcation properties for the coupled system (α = 1.5): (**a**) bifurcation diagram of the average vibration displacement; (**b**) bifurcation diagram of the average vibration velocity.

Figure 14 shows the motion phase diagrams of the coupled system corresponding to the resonance frequencies of Figure 13. In the case of a given α, the amplitudes of the resonance displacement and resonance velocity of the unit and the raft frame generally tend to decrease with the decrease in β. From the perspective of motion form, the motion phase diagram of the unit is approximately a closed ellipse, that is, it is approximately a harmonic vibration. The motion phase diagram of the raft frame has obvious irregularity, indicating that it contains strong superharmonic components. The motion phase diagram at the connection points of the lower vibration isolators with the cylindrical shell is the most complex, and with the decrease in β, the stability of the phase diagram orbits deteriorates and tends to be messy or even chaotic.

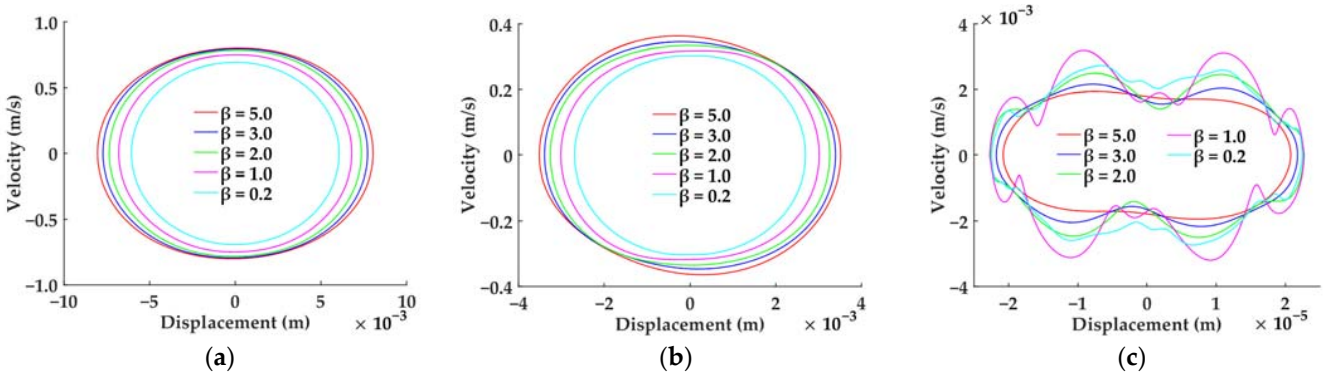

Figure 14. Effect of the length variation of the approximate linear working interval on the low-frequency vibration modes for the coupled system (α = 1.5): (**a**) motion phase diagram at the connection points of the upper vibration isolators with the unit A_1; (**b**) motion phase diagram at the connection points of the lower vibration isolators with the raft frame; (**c**) motion phase diagram at the connection points of the lower vibration isolators with the cylindrical shell.

Figure 15 shows the transmitted power flow spectrum in the coupled system when α is 1.5 and β is 5.0, 3.0, 2.0, 1.0, and 0.2, respectively. Comparing Figure 15 with Figure 12, it can be seen that the effect of reducing β is similar to that of increasing α. Both of them enhance the nonlinear hardening stiffness effect and make the resonance region move to the higher

frequency for the coupled system. Increasing α leads to a larger range of fundamental frequency variation of the system. But decreasing β extends the effect of nonlinear stiffness characteristics to higher frequencies. For example, when α is equal to 1.5 and β is equal to 0.2 in Figure 15, the effect of the nonlinear hardening characteristics of the vibration isolators extends significantly to higher frequency bands, increasing the transmitted power flow level on the band after the fundamental frequency for the coupled system.

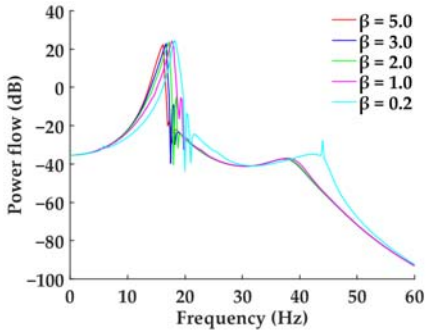

Figure 15. Effect of the length variation of the approximate linear working interval on the vibro-acoustic transfer characteristics for the coupled system (α = 1.5).

4. Conclusions

The present study was designed to study the effect of support stiffness nonlinearity on the low-frequency vibro-acoustic characteristics for the mechanical equipment—floating raft–cylindrical shell—underwater acoustic field coupled system. Firstly, the state space equations were established for the coupled system containing the vibration isolation supports with nonlinear stiffness characteristics, and in this process, the modal parameter identification method was deduced theoretically and verified by numerical simulation for the cylindrical shell—underwater acoustic field coupled subsystem. Then, the nonlinear stiffness constitutive relation was expressed in general by the softening and hardening characteristics for the vibration isolation supports, and the calculation formulas of the transmitted power flow in the nonlinear vibration isolation system were deduced. Finally, applying the Runge—Kutta method for the dynamics simulation, the effect of the variation of the nonlinear stiffness characteristics parameters on the low-frequency vibration modes and vibro-acoustic transfer characteristics was analyzed and discussed for the coupled system. The main findings are as follows:

1. For the coupled system with a nonlinear softening stiffness characteristic of the vibration isolation supports, the steady state vibration mode under harmonic excitation is single-periodic motion, but the superharmonic phenomenon is common. And the smaller the stiffness ratio is, the more superharmonic components are and the more complex the vibration form is. Compared with the linear stiffness case, the softening nonlinear stiffness can reduce the fundamental frequency and decrease the low-frequency vibro-acoustic transmission level within and after the resonance region for the vibration isolation system. And the stronger the softening characteristic is, the more significant the above effect is;
2. For the coupled system with a nonlinear hardening stiffness characteristic of the vibration isolation supports, the vibration mode under harmonic excitation is single-periodic motion at most frequencies, and the existence of superharmonics is its main vibration feature. And the larger the stiffness ratio is, the more superharmonic components are and the more complex the vibration form is. In a frequency band slightly higher than the fundamental frequency, it may show a nonperiodic motion mode (quasi-periodic or chaotic). Compared with the linear stiffness case, the hardening nonlinear stiffness can increase the fundamental frequency, broaden the resonance band and slightly raise the low-frequency vibro-acoustic transmission level within

and after the resonance region for the vibration isolation system. And the stronger the hardening characteristic is, the more significant the above effect is;

3. For the determined nonlinear stiffness ratio, the variation of the length of the approximate linear working interval has no effect on the periodicity of the vibration of the coupled system. For the coupled system with a nonlinear softening stiffness characteristic of the vibration isolation supports, the smaller the length of the approximately linear working interval is, the lower the low-frequency vibro-acoustic transfer level after the fundamental frequency resonance region is; while for the coupled system with a nonlinear hardening stiffness characteristic of the vibration isolation supports, the smaller the length of the approximately linear working interval is, the higher the low-frequency vibro-acoustic transfer level after the fundamental frequency resonance region is.

Author Contributions: Conceptualization, L.W. and R.H.; methodology, L.W. and R.H.; software, L.W. and R.H.; validation, L.W.; formal analysis, L.W. and R.H.; investigation, L.W.; resources, R.H.; data curation, L.W. and R.H.; writing—original draft preparation, L.W.; writing—review and editing, L.W. and R.H.; visualization, L.W.; supervision, R.H.; project administration, R.H.; funding acquisition, R.H. All authors have read and agreed to the published version of the manuscript.

Funding: This research received no external funding.

Data Availability Statement: The data used to support the findings of this study are available from the corresponding author upon request.

Conflicts of Interest: The authors declare no conflict of interest.

Appendix A. State Space Model of the Cylindrical Shell—Underwater Acoustic Field Coupled Subsystem

Appendix A.1. Solutions of the Admittance Functions for the Coupled Subsystem

A cylindrical coordinate system $Or\phi z$ is established on the middle surface of the cylindrical shell. Let the coordinate origin be located at the center of the left end face of the cylindrical shell, r and z be the distance from the spatial point $\sigma(r, \phi, z)$ to the central axis of the cylindrical shell and the left end face, respectively, and ϕ be the angle of $\sigma(r, \phi, z)$ deviating from the vertical direction. The transformation relationship between the cylindrical coordinates and the rectangular coordinates: $x = r\cos\phi$, $y = r\sin\phi$, $z = z$.

Let the length, thickness, and central radius of the cylindrical shell be L, d, and a, respectively, and the density, elastic modulus, and Poisson's ratio of the material of the cylindrical shell be ρ, E, and μ, respectively. A harmonic excitation force $F_z \cdot e^{j\omega t}$along the Oz axis direction is applied to the inside of the cylindrical shell at $\sigma_e(\varphi_e, z_e)$. Let $u(z, \phi, t) = U(z, \phi) \cdot e^{j\omega t}$, $v(z, \phi, t) = V(z, \phi) \cdot e^{j\omega t}$, and $w(z, \phi, t) = W(z, \phi) \cdot e^{j\omega t}$ denote the vibration displacement of the point $\sigma(\phi, z)$ on the cylindrical shell in z, ϕ, and r coordinate directions, respectively. Then, u, v, and w satisfy the following differential equations of motion:

$$\begin{cases} S_1(u,v,w) + \rho d \cdot \partial^2 u/\partial t^2 = F_z \cdot \delta(\varphi - \varphi_e) \cdot \delta(z - z_e) \cdot e^{j\omega t} \\ S_2(u,v,w) + \rho d \cdot \partial^2 v/\partial t^2 = 0 \\ S_3(u,v,w) + \rho d \cdot \partial^2 w/\partial t^2 = -p(r,\varphi,z)|_{r=a} \end{cases} \tag{A1}$$

where p is the radiated underwater acoustic pressure generated outside the cylindrical shell due to its vibration; S_1, S_2, and S_3 are differential operators, and

$$\begin{cases} S_1(U,V,W) = -\frac{Ed}{1-\mu^2}\left[\left(\frac{\partial^2}{\partial z^2} + \frac{1-\mu}{2a^2}\frac{\partial^2}{\partial \varphi^2}\right)U + \frac{1+\mu}{2a}\frac{\partial^2 V}{\partial z \partial \varphi} + \frac{\mu}{a}\frac{\partial W}{\partial z}\right] \\ S_2(U,V,W) = -\frac{Ed}{1-\mu^2}\left[\frac{1+\mu}{2a}\frac{\partial^2 U}{\partial z \partial \varphi} + \left(\frac{1-\mu}{2}\frac{\partial^2}{\partial z^2} + \frac{1}{a^2}\frac{\partial^2}{\partial \varphi^2}\right)V + \frac{1}{a^2}\frac{\partial}{\partial \varphi}\left(1 - \frac{d^2}{12}\nabla^2\right)W\right] \\ S_3(U,V,W) = \frac{Ed}{1-\mu^2}\left[\frac{\mu}{a}\frac{\partial U}{\partial z} + \frac{1}{a^2}\frac{\partial}{\partial \varphi}\left(1 - \frac{d^2}{12}\nabla^2\right)V + \left(\frac{1}{a^2} + \frac{d^2}{12}\nabla^4\right)W\right] \end{cases} \tag{A2}$$

where $\nabla^2 = \frac{\partial^2}{\partial z^2} + \frac{1}{a^2}\frac{\partial^2}{\partial \varphi^2}$, $\nabla^4 = \frac{\partial^4}{\partial z^4} + \frac{2}{a^2}\frac{\partial^4}{\partial z^2 \partial \varphi^2} + \frac{1}{a^4}\frac{\partial^4}{\partial \varphi^4}$.

The pressure $p = P(r, \phi, z)\cdot e^{j\omega t}$ of the underwater acoustic field outside the cylindrical shell satisfies the Helmholtz equation:

$$\nabla^2 P + k^2 P = 0 \tag{A3}$$

There are boundary conditions on the interface between the cylindrical shell and the external underwater acoustic field:

$$\left.\frac{\partial P}{\partial r}\right|_{r=a} = \begin{cases} \rho_0 \omega^2 \sum\limits_{j=0,k=1}^{\infty} \sum\limits_{l=1}^{3} q_{jki} H_{jkl}^{w} \cos[j(\varphi - \varphi_e)] \sin\left(\frac{k\pi z}{L}\right) \ (0 \le z \le L) \\ 0 \ (z < 0 \text{ or } z > L) \end{cases} \tag{A4}$$

where ρ_0 is the density of the acoustic field medium; H_{jk} (j, k = 1, 2, 3, 4) denotes a displacement admittance function, which means that when a unit excitation is applied along the direction of the support force at the connection point σ_k of the support and the cylindrical shell, the displacement response is generated at the connection point σ_j.

The displacement admittance matrix of the cylindrical shell—underwater acoustic field coupled subsystem is denoted by:

$$H(j\omega) = \left[H_{jk}\right]_{4\times 4} \tag{A5}$$

For the calculation of the admittance functions of the cylindrical shell—underwater acoustic field coupled subsystem, see also Equations (11)–(18) in [33]. It can be seen from these equations that, due to the complexity of the calculation formulas, only discrete numerical solutions of the admittance functions can be given. Figure A1 shows examples of calculated results for the admittance functions of the cylindrical shell along the support direction (taking H_{11}, H_{12}, and H_{14} as examples).

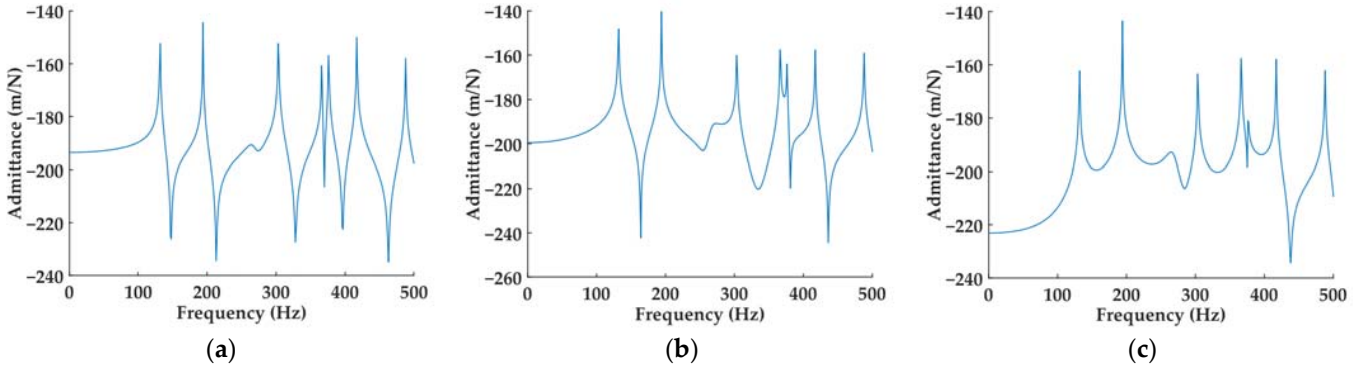

Figure A1. Examples of the calculation results for the admittance along the support direction: (**a**) H_{11}; (**b**) H_{12}; (**c**) H_{14}.

Appendix A.2. Modal Parameter Identification of the Coupled Subsystem

Since the main focus is on low-frequency vibration problems in this paper, only the first f-order modes are intercepted. Also, the admittance function is expressed as a ratio of two polynomial functions:

$$H_{jk}(\mathrm{j}\omega) \approx \frac{a_m(\mathrm{j}\omega)^{m-1} + a_{m-1}(\mathrm{j}\omega)^{m-2} + \cdots + a_2(\mathrm{j}\omega) + a_1}{(\mathrm{j}\omega)^{n-1} + b_{n-1}(\mathrm{j}\omega)^{n-2} + \cdots + b_2(\mathrm{j}\omega) + b_1} \tag{A6}$$

where j, k = 1, 2, 3, 4; $n = 2f + 1$, $m = 2f - 1$.

Let $\hat{H}_{jk}(\mathrm{j}\omega)$ be the discrete numerical spectrum of $H_{jk}(\mathrm{j}\omega)$ obtained by theoretical calculation, and for a number of frequencies ω_1, ω_2,ω_3, …, ω_N, there are $\hat{H}_{jk,i} = \hat{H}_{jk}(\mathrm{j}\omega_i)$, ($i$ = 1, 2, …, N). Noting that $\boldsymbol{a} = [a_1, a_2, \ldots, a_m]^{\mathrm{T}}$, $\boldsymbol{b} = [b_1, b_2, \ldots, b_{n-1}]^{\mathrm{T}}$, $\boldsymbol{p}_i = [1, \mathrm{j}\omega_i, \ldots,$

$(\mathrm{j}\omega_i)^{m-1}]$, $\boldsymbol{q}_i = \hat{H}_{jk,i}\,[1, \mathrm{j}\omega_i, \ldots, (\mathrm{j}\omega_i)^{n-2}]$, $h_i = (\mathrm{j}\omega_i)^{n-1}\,\hat{H}_{jk,i}$, $\boldsymbol{e}_i = \boldsymbol{p}_i\boldsymbol{a} - \boldsymbol{q}_i\boldsymbol{b} - h_i$, $\boldsymbol{P} = [\boldsymbol{p}_1, \boldsymbol{p}_2, \ldots, \boldsymbol{p}_s]^{\mathrm{T}}$, $\boldsymbol{Q} = [\boldsymbol{q}_1, \boldsymbol{q}_2, \ldots, \boldsymbol{q}_s]^{\mathrm{T}}$, and $\boldsymbol{h} = [h_1, h_2, \ldots, h_s]^{\mathrm{T}}$, the matrix expression and the total mean squared error can be obtained:

$$\boldsymbol{e} = \boldsymbol{P}\boldsymbol{a} - \boldsymbol{Q}\boldsymbol{b} - \boldsymbol{h} \tag{A7}$$

$$J = \boldsymbol{e}^{\mathrm{T}}\boldsymbol{e}^{*} = \boldsymbol{x}^{\mathrm{T}}\boldsymbol{A}_{\mathrm{R}}\boldsymbol{x} - 2\boldsymbol{B}\boldsymbol{x} + |\boldsymbol{h}|^2 \tag{A8}$$

where the superscript '*' represents conjugation relation; $\boldsymbol{x} = \begin{bmatrix}\boldsymbol{a}\\ \boldsymbol{b}\end{bmatrix}$, $\boldsymbol{A} = \begin{bmatrix}\boldsymbol{P}^{\mathrm{T}}\boldsymbol{P}^{*} & -\boldsymbol{P}^{\mathrm{T}}\boldsymbol{Q}^{*}\\ -\boldsymbol{Q}^{\mathrm{T}}\boldsymbol{P}^{*} & \boldsymbol{Q}^{\mathrm{T}}\boldsymbol{Q}^{*}\end{bmatrix}$, $\boldsymbol{B} = \left[\boldsymbol{h}_{\mathrm{R}}^{\mathrm{T}}\boldsymbol{P}_{\mathrm{R}} + \boldsymbol{h}_{\mathrm{I}}^{\mathrm{T}}\boldsymbol{P}_{I} - \left(\boldsymbol{h}_{\mathrm{R}}^{\mathrm{T}}\boldsymbol{Q}_{R} + \boldsymbol{h}_{\mathrm{I}}^{\mathrm{T}}\boldsymbol{Q}_{I}\right)\right]$, $\boldsymbol{P}_{\mathrm{R}}$ and $\boldsymbol{P}_{\mathrm{I}}$ are the real and imaginary parts of $\boldsymbol{P}$, respectively; $\boldsymbol{Q}_{\mathrm{R}}$ and $\boldsymbol{Q}_{\mathrm{I}}$ are the real and imaginary parts of $\boldsymbol{Q}$, respectively; $\boldsymbol{h}_{\mathrm{R}}$ and $\boldsymbol{h}_{\mathrm{I}}$ are the real and imaginary parts of $\boldsymbol{h}$, respectively; $\boldsymbol{A}_{\mathrm{R}}$ is the real part of $\boldsymbol{A}$.

Consider the total mean squared error $\boldsymbol{J}$ as a function of $\boldsymbol{x}$. To obtain a minimum of $\boldsymbol{J}$, let the gradient of Equation (A8) to $\boldsymbol{x}$ be 0:

$$\nabla\boldsymbol{J} = \boldsymbol{A}_{\mathrm{R}}\boldsymbol{x} - \boldsymbol{B}^{\mathrm{T}} = \boldsymbol{0} \Rightarrow \boldsymbol{x} = \boldsymbol{A}_{\mathrm{R}}^{-1}\boldsymbol{B}^{\mathrm{T}} \tag{A9}$$

The polynomial coefficients of the admittance function numerator and denominator can be fitted using the above equation.

Appendix A.3. Establishment of State Space Equation for the Coupled Subsystem

For a continuous structure, its vibration displacement response $w(\sigma, t)$ can be expressed in the form of vibration model superposition:

$$w(\sigma, t) = \sum_{i=1}^{\infty}\psi_i(\sigma)q_i(t) \tag{A10}$$

where $\psi_i(\sigma)$ is the ith-order vibration mode function and $q_i(t)$ is the ith-order modal coordinate.

A modal damping ratio ξ_i is introduced, and the modal coordinate equation is obtained by using the orthogonality of the vibration mode function:

$$\ddot{q}_i + 2\xi_i\omega_i\dot{q}_i + \omega_i^2 q_i = \sum_{j=1}^{4}F_j(t)\overline{\psi}_i(\sigma_j),\ (i = 1, 2, \ldots) \tag{A11}$$

where ω_i is the i-th order modal frequency; $F_j(t)$ is the concentrated excitation force of the cylindrical shell subjected to the support at point σ_j (j = 1, 2, 3, 4); $\overline{\psi}_i = \psi_i/\sqrt{M_i}$ is the regular vibration mode function; $M_i = \int_{\Sigma} m_{\Sigma}\psi_i^2(\sigma)\mathrm{d}\sigma$ is the i-th order modal mass, m_{Σ} is the areal density.

According to Equations (A10) and (A11), the admittance function can be expressed as:

$$H_{jk}(\mathrm{j}\omega) \approx \sum_{i=1}^{f}\frac{\overline{\psi}_i(\sigma_{\mathrm{j}})\overline{\psi}_i(\sigma_k)}{\mathrm{j}2\sqrt{1-\xi_i^2}\omega_i}\left(\frac{1}{\mathrm{j}\omega + \xi_i\omega_i - \mathrm{j}\sqrt{1-\xi_i^2}\omega_i} - \frac{1}{\mathrm{j}\omega + \xi_i\omega_i + \mathrm{j}\sqrt{1-\xi_i^2}\omega_i}\right) \tag{A12}$$

According to the above relation, if $\boldsymbol{H}(\mathrm{j}\omega)$ is known, each $H_{jk}(\mathrm{j}\omega)$ has the same poles $s_i = -\xi_i\omega_i + \mathrm{j}\sqrt{1-\xi_i^2}\omega_i$, ($i$ = 1, 2, …, f). Since $|s_i| = \omega_i$, the poles are sorted by $|s_1| < |s_2| < |s_3| < \ldots$, and the modal parameters are determined as follows:

$$\omega_i = |s_i|,\ \xi_i = -\mathrm{Re}\{s_i\}/|s_i| \tag{A13}$$

$$\overline{\psi}_i(\sigma_1) = \sqrt{\mathrm{j}2\mathrm{Im}\{s_i\}\cdot[H_{11}\cdot(\mathrm{j}\omega - s_i)]_{\mathrm{j}\omega = s_i}} \tag{A14}$$

$$\overline{\psi}_i(\sigma_j) = \frac{\mathrm{j2Im}\{s_i\}\cdot\left[H_{j1}\cdot(\mathrm{j}\omega - s_i)\right]_{\mathrm{j}\omega=s_i}}{\overline{\psi}_i(\sigma_1)} = \sqrt{\frac{\mathrm{j2Im}\{s_i\}}{\left[H_{11}\cdot(\mathrm{j}\omega - s_i)\right]_{\mathrm{j}\omega=s_i}}}\left[H_{j1}\cdot(\mathrm{j}\omega - s_i)\right]_{\mathrm{j}\omega=s_i} \tag{A15}$$

Substituting the above relations into Equations (A11) and (A10), the modal coordinate equation and the modal superposition formula of vibration displacement expressed in terms of the admittance functions are obtained:

$$\ddot{q}_i - 2\mathrm{Re}\{s_i\}\dot{q}_i + |s_i|^2 q_i = \sqrt{\mathrm{j2Im}\{s_i\}}\sum_{j=1}^{4} F_j(t)\frac{\left[H_{j1}\cdot(j\omega - s_i)\right]_{\mathrm{j}\omega=s_i}}{\sqrt{\left[H_{11}\cdot(\mathrm{j}\omega - s_i)\right]_{\mathrm{j}\omega=s_i}}},\ (i = 1, 2, \ldots, f) \tag{A16}$$

$$w(\sigma_j, t) = \sum_{i=1}^{f} q_i(t)\sqrt{\frac{\mathrm{j2Im}\{s_i\}}{\left[H_{11}\cdot(\mathrm{j}\omega - s_i)\right]_{\mathrm{j}\omega=s_i}}}\left[H_{j1}\cdot(\mathrm{j}\omega - s_i)\right]_{\mathrm{j}\omega=s_i},\ (j = 1, 2, 3, 4) \tag{A17}$$

The above theories are based on proportional damping assumption, and the vibration mode function is a real function by default. But applying Equation (A14) in practical analysis mostly yields complex numbers, that is, complex modes appear. If the complex modes are substituted into Equations (A11) or (A16), the modal coordinate equation will be made to have complex terms, and ultimately the displacement response obtained from Equation (A17) will also become a complex number, which is inconsistent with its physical meaning. Considering the universality of complex modes in this kind of problem, Equations (A11), (A12), and (A17) are modified as:

$$H_{jk}(\mathrm{j}\omega) \approx \sum_{i=1}^{f}\frac{\overline{\phi}_{ij}\overline{\phi}_{ik}}{\mathrm{j}\omega - s_i} + \sum_{i=1}^{f}\frac{\overline{\phi}_{ij}^{*}\overline{\phi}_{ik}^{*}}{\mathrm{j}\omega - s_i^{*}} \tag{A18}$$

$$\begin{bmatrix}\dot{v}_1\\ \vdots\\ \dot{v}_f\\ \dot{v}_1^{*}\\ \vdots\\ \dot{v}_f^{*}\end{bmatrix} - \begin{bmatrix}s_1 & & & & & \\ & \ddots & & & & \\ & & s_f & & & \\ & & & s_1^{*} & & \\ & & & & \ddots & \\ & & & & & s_f^{*}\end{bmatrix}\begin{bmatrix}v_1\\ \vdots\\ v_f\\ v_1^{*}\\ \vdots\\ v_f^{*}\end{bmatrix} = \begin{bmatrix}\sum_{j=1}^{4}\overline{\phi}_{1j}F_j(t)\\ \vdots\\ \sum_{j=1}^{4}\overline{\phi}_{fj}F_j(t)\\ \sum_{j=1}^{4}\overline{\phi}_{1j}^{*}F_j(t)\\ \vdots\\ \sum_{j=1}^{4}\overline{\phi}_{fj}^{*}F_j(t)\end{bmatrix} \tag{A19}$$

$$w(\sigma_j, t) = \sum_{i=1}^{f} 2\left[\mathrm{Re}\{v_i(t)\}\cdot\mathrm{Re}\left\{\overline{\phi}_{ij}\right\} - \mathrm{Im}\{v_i(t)\}\cdot\mathrm{Im}\left\{\overline{\phi}_{ij}\right\}\right],\ (j = 1, 2, 3, 4) \tag{A20}$$

where the poles s_i and s_i^{*} (i = 1, 2, …, f) are the f pairs of conjugate latent roots obtained in solving the eigenvalue problem for the state space equation; v_i is obtained by variable substitution $\boldsymbol{q} = \boldsymbol{\Phi v}$;$\boldsymbol{\Phi}$ is a complex modal matrix consisting of $\boldsymbol{\Phi}_i$ and $\boldsymbol{\Phi}_i^{*}$; $\boldsymbol{\Phi}_i$ and $\boldsymbol{\Phi}_i^{*}$ are complex eigenvectors corresponding to s_i and s_i^{*}; $\overline{\phi}_{ij}$ is obtained by using the residue method, $\overline{\phi}_{ij} = \frac{H_{j1}\cdot(\mathrm{j}\omega - s_i)\big|_{\mathrm{j}\omega=s_i}}{\sqrt{H_{11}\cdot(\mathrm{j}\omega - s_i)|_{\mathrm{j}\omega=s_i}}}$ and $\overline{\phi}_{ij}^{*} = \frac{H_{j1}\cdot\left(\mathrm{j}\omega - s_i^{*}\right)\big|_{\mathrm{j}\omega=s_i^{*}}}{\sqrt{H_{11}\cdot\left(\mathrm{j}\omega - s_i^{*}\right)\big|_{\mathrm{j}\omega=s_i^{*}}}}$.

The upper part and the lower part of Equation (A19) are repeated (conjugate relation), so only the upper part is abbreviated to a state space equation:

$$\dot{\boldsymbol{u}}_{\mathrm{C}} = \boldsymbol{S}_{\mathrm{C}}\boldsymbol{u}_{\mathrm{C}} + \overline{\boldsymbol{\Phi}}_{\mathrm{C}}\boldsymbol{F}_{\mathrm{y}} \tag{A21}$$

where $\boldsymbol{u}_C = [u_{C1}, u_{C2}, u_{C3}, \ldots, u_{Cf}]^T$ is a state variable; $\boldsymbol{F}_y = [F_{y1}, F_{y2}, F_{y3}, F_{y4}]^T$ is an excitation force column vector of the connection supports to the cylindrical shell; $\boldsymbol{S}_C = \mathrm{diag}[s_{C1}, s_{C2}, s_{C3}, \ldots, s_{Cf}]$ is a diagonal matrix composed of poles (sorted by $|s_{C1}| < |s_{C2}| < |s_{C3}| < \ldots < |s_{Cf}|$); $\overline{\boldsymbol{\Phi}}_C$ is a matrix consisting of the modal parameter $\overline{\phi}_{ij}$, and

$$\overline{\boldsymbol{\Phi}}_C = \begin{bmatrix} \overline{\phi}_{11} & \overline{\phi}_{12} & \overline{\phi}_{13} & \overline{\phi}_{14} \\ \overline{\phi}_{21} & \overline{\phi}_{22} & \overline{\phi}_{23} & \overline{\phi}_{24} \\ \overline{\phi}_{31} & \overline{\phi}_{32} & \overline{\phi}_{33} & \overline{\phi}_{34} \\ \vdots & \vdots & \vdots & \vdots \\ \overline{\phi}_{f1} & \overline{\phi}_{f2} & \overline{\phi}_{f3} & \overline{\phi}_{f4} \end{bmatrix} \tag{A22}$$

The functional relation between $\boldsymbol{w}_{yj}$ and the state space variable $\boldsymbol{u}_C$ is

$$\boldsymbol{w}_y = 2\mathrm{Re}\left\{\overline{\boldsymbol{\Phi}}_C^T \boldsymbol{u}_C\right\} = 2\left(\mathrm{Re}\left\{\overline{\boldsymbol{\Phi}}_C^T\right\} \cdot \mathrm{Re}\{\boldsymbol{u}_C\} - \mathrm{Im}\left\{\overline{\boldsymbol{\Phi}}_C^T\right\} \cdot \mathrm{Im}\{\boldsymbol{u}_C\}\right) \tag{A23}$$

where $\boldsymbol{w}_y = [w_{y1}, w_{y2}, w_{y3}, w_{y4}]^T$.

Appendix B. Control Parameters in Simulation Calculation

MATLAB is used in the simulation calculation in this paper. The specific theory of mathematical operations has been described in detail in Section 2 and Appendix A. Here, some control parameters related to computational convergence are supplemented.

As mentioned above, the displacement response of the coupled system at any time t_1 is $\boldsymbol{w}_{A1} = [w_{A1}, w_{A2}, w_{A3}, w_{A4}]^T$, $\boldsymbol{w}_{A2} = [w_{A5}, w_{A6}, w_{A7}, w_{A8}]^T$, $\boldsymbol{w}_t = [w_{t1}, w_{t2}, w_{t3}, w_{t4}, w_{t5}, w_{t6}, w_{t7}, w_{t8}]^T$, $\boldsymbol{w}_b = [w_{b1}, w_{b2}, w_{b3}, w_{b4}]^T$, and $\boldsymbol{w}_y = [w_{y1}, w_{y2}, w_{y3}, w_{y4}]^T$. The above displacement responses are assembled into a total displacement vector $\boldsymbol{w} = \left[\boldsymbol{w}_{A1}^T, \boldsymbol{w}_{A2}^T, \boldsymbol{w}_t^T, \boldsymbol{w}_b^T, \boldsymbol{w}_y^T\right]^T$, whose corresponding velocity vector is $\dot{\boldsymbol{w}}$. Suppose there is a time $t_2 = t_1 + T$, the displacement response is $\boldsymbol{w}'$, and the velocity response is $\dot{\boldsymbol{w}}'$. Considering $\boldsymbol{w}'$ and $\dot{\boldsymbol{w}}'$ as two points in phase space, according to Poincaré mapping theory, if these two points can coincide, then the system has a period T. However, due to the error caused by the precision of numerical calculation, it is difficult to strictly meet this condition. Therefore, a tolerance criterion ε is set so that:

$$\frac{\left\|\boldsymbol{w}' - \boldsymbol{w}\right\|_2}{\left\|\boldsymbol{w}'\right\|_2} < \varepsilon \tag{A24}$$

If the displacement responses w and $\boldsymbol{w}'$ satisfy the above condition, the calculation is considered to be convergent, that is, the motion of the system is periodic (T is a period). Otherwise, it is divergent, that is, the motion of the system is nonperiodic (quasi-periodic or chaotic).

Similarly, the velocity responses $\dot{\boldsymbol{w}}$ and $\dot{\boldsymbol{w}}'$ should also satisfy the condition, that is:

$$\frac{\left\|\dot{\boldsymbol{w}}' - \dot{\boldsymbol{w}}\right\|_2}{\left\|\dot{\boldsymbol{w}}'\right\|_2} < \varepsilon \tag{A25}$$

The above tolerance criterion ε is set to 1.0×10^{-5} in the simulation example of this paper.

Figure A2 shows the convergence process of simulation calculation under $\alpha = 0.5$ and $\beta = 1.0$ as an example of the connection points of the upper vibration isolators with unit A_1. It can be seen from Figure A2a,b that convergence is obtained when $t = 1.7$ s. Figure A2c shows a sequence of state as it move to the attractor.

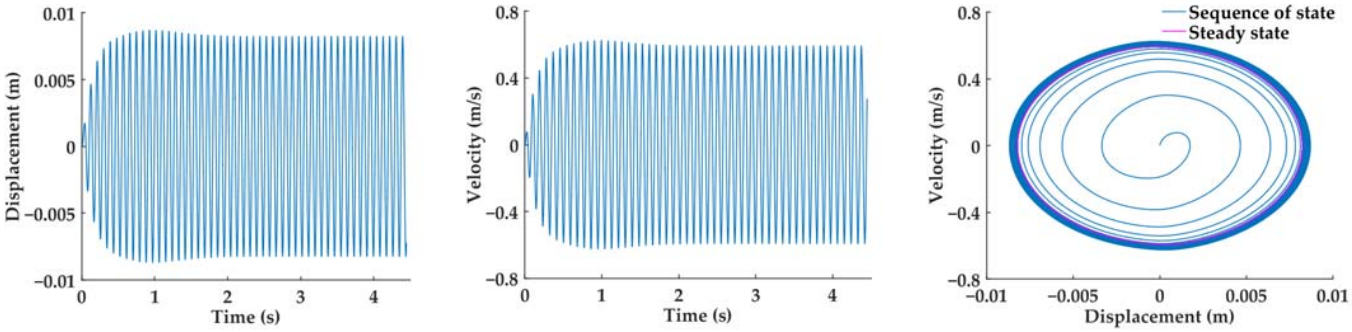

Figure A2. The convergence process of the calculation at the connection points of the upper vibration isolators with the unit A_1 ($\alpha = 0.5$, $\beta = 1.0$): (**a**) time that the displacement response calculation took to obtain convergence; (**b**) time that the velocity response calculation took to obtain convergence; (**c**) the sequence of state as it moves to the attractor.

Similarly, at the connection points of the upper vibration isolators with the unit A_2, the upper vibration isolators with the raft frame, the lower vibration isolators with the raft frame, and the lower vibration isolators with the cylindrical shell, and under other nonlinear stiffness conditions, simulation calculation of the periodic motion has similar convergence properties, which will not be shown here one by one.

References

1. Smirnov, V.; Mondrus, V. Comparison of linear and nonlinear vibration isolation system under random excitation. *Procedia Eng.* **2016**, *153*, 673–678. [CrossRef]
2. Santhosh, B. Dynamics and performance evaluation of an asymmetric nonlinear vibration isolation mechanism. *J. Braz. Soc. Mech. Sci. Eng.* **2018**, *40*, 169. [CrossRef]
3. Dutta, S.; Chakraborty, G. Performance analysis of nonlinear vibration isolator with magneto-rheological damper. *J. Sound Vib.* **2014**, *333*, 5097–5114. [CrossRef]
4. Suman, S.; Balaji, P.S.; Selvakumar, K.; Kumaraswamidhas, L.A. Nonlinear vibration control device for a vehicle suspension using negative stiffness mechanism. *J. Vib. Eng. Technol.* **2021**, *9*, 957–966. [CrossRef]
5. Araki, Y.; Asai, T.; Kimura, K.; Maezawa, K.; Masui, T. Nonlinear vibration isolator with adjustable restoring force. *J. Sound Vib.* **2013**, *332*, 6063–6077. [CrossRef]
6. Zhao, F.; Ji, J.C.; Ye, K.; Luo, Q. Increase of quasi-zero stiffness region using two pairs of oblique springs. *Mech. Syst. Signal Process.* **2020**, *144*, 106975. [CrossRef]
7. Zhao, F.; Ji, J.C.; Ye, K.; Luo, Q. An innovative quasi-zero stiffness isolator with three pairs of oblique springs. *Int. J. Mech. Sci.* **2021**, *192*, 106093. [CrossRef]
8. Ye, K.; Ji, J.C.; Brown, T. Design of a quasi-zero stiffness isolation system for supporting different loads. *J. Sound Vib.* **2020**, *471*, 115198. [CrossRef]
9. Chang, Y.; Zhou, J.; Wang, K.; Xu, D. A quasi-zero-stiffness dynamic vibration absorber. *J. Sound Vib.* **2021**, *494*, 115859. [CrossRef]
10. Bouna, H.S.; Nbendjo, B.R.N.; Woafo, P. Isolation performance of a quasi-zero stiffness isolator in vibration isolation of a multi-span continuous beam bridge under pier base vibrating excitation. *Nonlinear Dyn.* **2020**, *100*, 1125–1141. [CrossRef]
11. Drezet, C.; Kacem, N.; Bouhaddi, N. Design of a nonlinear energy harvester based on high static low dynamic stiffness for low frequency random vibrations. *Sens. Actuators A Phys.* **2018**, *283*, 54–64. [CrossRef]
12. Lu, Z.; Wu, D.; Ding, H.; Chen, L. Vibration isolation and energy harvesting integrated in a Stewart platform with high static and low dynamic stiffness. *Appl. Math. Model.* **2021**, *89*, 249–267. [CrossRef]
13. Hao, R.; Lu, Z.; Ding, H.; Chen, L. Orthogonal six-DOFs vibration isolation with tunable high-static-low-dynamic stiffness: Experiment and analysis. *Int. J. Mech. Sci.* **2022**, *222*, 107237. [CrossRef]
14. Hao, R.; Lu, Z.; Ding, H.; Chen, L. A nonlinear vibration isolator supported on a flexible plate: Analysis and experiment. *Nonlinear Dyn.* **2022**, *108*, 941–958. [CrossRef]
15. Sun, Y.; Zhou, J.; Thompson, D.; Yuan, T.; Gong, D.; You, T. Design, analysis and experimental validation of high static and low dynamic stiffness mounts based on target force curves. *Int. J. Non-Linear Mech.* **2020**, *126*, 103559. [CrossRef]
16. Yao, Y.; Li, H.; Li, Y.; Wang, X. Analytical and experimental investigation of a high-static-low-dynamic stiffness isolator with cam-roller-spring mechanism. *Int. J. Mech. Sci.* **2020**, *186*, 105888. [CrossRef]
17. Chong, X.; Wu, Z.; Li, F. Vibration isolation properties of the nonlinear X-combined structure with a high-static and low-dynamic stiffness: Theory and experiment. *Mech. Syst. Signal Process.* **2022**, *179*, 109352. [CrossRef]

18. Leutcho, G.D.; Kengne, J. A unique chaotic snap system with a smoothly adjustable symmetry and nonlinearity: Chaos, offset-boosting, antimonotonicity, and coexisting multiple attractors. *Chaos Solitons Fractals* **2018**, *113*, 275–293. [CrossRef]
19. Yan, B.; Ma, H.; Jian, B.; Wang, K.; Wu, C. Nonlinear dynamics analysis of a bi-state nonlinear vibration isolator with symmetric permanent magnets. *Nonlinear Dyn.* **2019**, *97*, 2499–2519. [CrossRef]
20. Rahman, Z.A.S.A.; Jasim, B.H. Hidden Dynamics Investigation, Fast Adaptive Synchronization, and Chaos-Based Secure Communication Scheme of a New 3D Fractional-Order Chaotic System. *Inventions* **2022**, *7*, 108. [CrossRef]
21. Li, Y.; Yi, Y.; Wu, J.; Gu, Y. A novel feature extraction method for ship-radiated noise based on hierarchical refined composite multi-scale dispersion entropy-based Lempel-Ziv complexity. *Deep Sea Res. Part I Oceanogr. Res. Pap.* **2023**, *199*, 104111. [CrossRef]
22. Karimov, A.; Rybin, V.; Dautov, A.; Karimov, T.; Bobrova, Y.; Butusov, D. Mechanical Chaotic Duffing System with Magnetic Springs. *Inventions* **2023**, *8*, 19. [CrossRef]
23. Dreau, J.; Magnain, B.; Batailly, A. Multi-element polynomial chaos expansion based on automatic discontinuity detection for nonlinear systems. *J. Sound Vib.* **2023**, *567*, 117920. [CrossRef]
24. Cassidy, I.L.; Scruggs, J.T. Nonlinear stochastic controllers for power-flow-constrained vibratory energy harvesters. *J. Sound Vib.* **2013**, *332*, 3134–3147. [CrossRef]
25. Silva, O.M.; Neves, M.M.; Jordan, R.; Lenzi, A. An FEM-based method to evaluate and optimize vibration power flow through a beam-to-plate connection. *J. Braz. Soc. Mech. Sci. Eng.* **2017**, *39*, 413–426. [CrossRef]
26. Varghese, C.K.; Shankar, K.K. Damage identification using combined transient power flow balance and acceleration matching technique. *Struct. Control. Health Monit.* **2014**, *21*, 135–155. [CrossRef]
27. Yang, J.; Xiong, Y.; Xing, J. Vibration power flow and force transmission behaviour of a nonlinear isolator mounted on a nonlinear base. *Int. J. Mech. Sci.* **2016**, *115*, 238–252. [CrossRef]
28. Shi, B.; Yang, J. Quantification of vibration force and power flow transmission between coupled nonlinear oscillators. *Int. J. Dyn. Control.* **2020**, *8*, 418–435. [CrossRef]
29. Ren, Y.; Chang, S.; Liu, G.; Wu, L.; Wang, H. Vibratory power flow analysis of a gear-housing-foundation coupled system. *Shock. Vib.* **2018**, *2018*, 5974759. [CrossRef]
30. Zhang, Y.; Zhou, L.; Wang, S.; Yang, T.; Chen, L. Vibration power flow characteristics of the whole-spacecraft with a nonlinear energy sink. *J. Low Freq. Noise Vib. Act. Control* **2019**, *38*, 341–351. [CrossRef]
31. Xu, D.; Du, J.; Zhao, Y. Flexural vibration and power flow analyses of axially loaded beams with general boundary and non-uniform elastic foundations. *Adv. Mech. Eng.* **2020**, *12*, 1687814020921719. [CrossRef]
32. Mahapatra, K.; Panigrahi, S.K. Effect of general coupling conditions on the vibration and power flow characteristics of a two-plate built-up plate structure. *Mech. Based Des. Struct. Mach.* **2021**, *49*, 841–861. [CrossRef]
33. Liu, S.; Huo, R.; Wang, L. Vibroacoustic Transfer Characteristics of Underwater Cylindrical Shells Containing Complex Internal Elastic Coupled Systems. *Appl. Sci.* **2023**, *13*, 3994. [CrossRef]
34. More, S.; Padmanabhan, C. Power flow based analysis of a floating raft vibration isolation system. *Am. Phys. Soc.* **2014**, *72*, 691–708.